

© 2010 Alexander Haak

EVALUATION OF THE ACCURACY AND PRECISION OF
ULTRASOUND ATTENUATION SLOPE ESTIMATES

BY

ALEXANDER HAAK

THESIS

Submitted in partial fulfillment of the requirements
for the degree of Master of Science in Electrical and Computer Engineering
in the Graduate College of the
University of Illinois at Urbana-Champaign, 2010

Urbana, Illinois

Adviser:

Professor William D. O'Brien, Jr.

ABSTRACT

New approaches in the field of ultrasound utilize the frequency content of the backscattered signal, which contains information about the scattering tissue structure and enables quantitative ultrasound imaging. The ultrasonic attenuation is a quantitative parameter that can be used to characterize tissue. Furthermore, for any scatterer size estimations, the spectral distortions caused by attenuation need to be corrected, and therefore the attenuation has to be measured in vivo to make such techniques applicable for medical imaging. There are two main techniques, spectral difference and spectral shift, used to estimate the attenuation from backscattered ultrasound data. In this work we focus on the spectral shift method, which utilizes the downshift of the center frequency of a pulse propagating through an attenuating medium. The spectral shift method is less sensitive than the spectral difference method and there has not been much work done on estimating the accuracy and precision of the attenuation estimates. The amount of downshift of the pulse depends on the square of the absolute bandwidth of the pulse and is believed to be a crucial parameter for the accuracy of the attenuation estimate. An algorithm utilizing the spectral shift method was implemented and tested on virtual and physical phantoms with different attenuation slopes. The virtual phantoms were interrogated with pulses with a wide range of center frequencies and fractional bandwidths. We found that the algorithm used to estimate the attenuation slope is unbiased but has a high variance in the estimates for situations where the amount of downshift of the pulse is small. Experiments with two transducers differing in absolute bandwidth indicated that for a fixed analysis depth higher bandwidths perform better.

To Mutsch

ACKNOWLEDGMENTS

I would like to acknowledge many, many people who helped and supported me through this not always easy process of education. First of all I would like to thank my adviser, Dr. William D. O'Brien Jr., for giving me the opportunity to do research in an interesting field, challenging me, giving me the freedom to explore on my own, and always supporting me in and outside academia. I also would like to thank Dr. Roberto Lavarello for those many interesting and insightful conversations. I wish to thank everyone in BRL who supported me with their great work and expertise, and who were enjoyable to work with. I also would like to thank my parents and my sister for their never ending support which made it possible for me to achieve all my goals. Thanks to the NIH for funding this research.

TABLE OF CONTENTS

CHAPTER 1 INTRODUCTION	1
1.1 Background	1
1.2 Motivation	1
1.3 Objectives	2
CHAPTER 2 THEORY	4
2.1 Attenuation of Sound Waves	4
2.2 Attenuation Mechanism	5
2.3 Attenuation in Biological Tissue	7
2.4 Estimation of Attenuation from Backscattered Sound	8
2.5 Simulation of an Attenuating Medium	13
2.6 Figures	15
CHAPTER 3 METHODOLOGY	17
3.1 Simulated RF Data	17
3.2 Physical Phantoms	18
3.3 RF data Acquisition Physical Phantoms	19
3.4 Attenuation Slope Estimation	20
3.5 Figures	22
CHAPTER 4 RESULTS AND DISCUSSION	27
4.1 Accuracy of the Gaussian Fit	27
4.2 Estimation Performance for a Distribution of Scatterers in an Attenuating Medium	29
4.3 Spatial Variation Noise	30
4.4 Attenuation Slope Estimates	31
4.5 Estimation Error for Different Attenuation Slopes	33
4.6 Attenuation Slope Estimates from Physical Phantoms	34
4.7 Figures	36
CHAPTER 5 CONCLUSION	67
APPENDIX A	69
A.1 Derivation of Gaussian Pulse Propagating through Lossy Medium	69
A.2 Fractional Bandwidth	70

REFERENCES 71

CHAPTER 1

INTRODUCTION

1.1 Background

Medical ultrasound is one imaging modality among others such as X-ray, computer tomography, or magnetic resonance imaging. Ultrasound imaging is inexpensive compared to the other modalities, can be highly portable, can image in real time, and uses non-ionizing radiation which does not damage tissue [1].

Conventional ultrasound imaging uses only the amplitude information of the backscattered signal to qualitatively visualize macroscopic tissue structure. The frequency content of the backscattered ultrasound contains information about the tissue microstructure which can be quantified [2, 3]. The quantitative information about the scattering sites may be used for diagnosing tissue diseases.

1.2 Motivation

Utilizing the backscattered frequency content in order to gain information about the scattering sites within the tissue makes it necessary to correct for attenuation. The local attenuation itself is also a parameter which can be used to diagnose tissue diseases in vivo [1, 4].

There are two main methods used to estimate the local attenuation from the backscattered signal. The first method utilizes the spectral differences of the spectral amplitude for spectra obtained at different depths [5]. When corrected for diffraction this method has a good sensitivity and the attenuation can be analyzed at different frequencies. However, inhomogeneities such as tissue boundaries can alter the attenuation

estimate and lead to wrong estimates [6].

The second method was introduced by Kuc et al. [7] and utilizes the downshift of the center frequency of a pulse to estimate the attenuation slope. Several assumptions are made with this approach. Firstly, the attenuation is assumed to change linearly with frequency, and secondly, the shape of the emitted pulse can be approximated by a Gaussian function. These assumptions constrain this approach to a limited set of applications. However, Kim et al. [6] argue that the spectral shift method will not suffer from inhomogeneities such as tissue boundaries since the spectral amplitude is not used to estimate attenuation, and is therefore superior to the spectral difference method even though they do not provide any evidence to support this statement. The spectral shift method is also less sensitive than the spectral difference method. There has not been a great deal of research on the accuracy and precision of the attenuation slope estimates using the spectral shift method. We hypothesize that with sufficient downshift of the pulse center frequency, accurate and precise attenuation slope estimates can be obtained. The downshift of the pulse center frequency depends upon other terms such as attenuation slope, penetration depth, and the square of the absolute bandwidth of the ultrasound source. Therefore, we believe that in order to obtain a certain accuracy and precision in the attenuation estimates for a defined analysis region, the right transducer bandwidth has to be chosen.

1.3 Objectives

In this work we are investigating the accuracy and precision of the spectral shift method. An estimation scheme utilizing the spectral shift method was written. Computer simulations were used to investigate the estimation performance of the algorithm for a series of pulses with different center frequencies and fractional bandwidths. The algorithm was also tested on virtual phantoms with different attenuation slopes and varied size of the region of analysis.

Physical phantoms mimicking the characteristics of soft tissue were scanned with single element transducers and the attenuation slope was estimated and compared to insertion loss measurements.

In Chapter 2 a theoretical discussion is given about the attenuation mechanism, the estimation scheme and the simulation scheme. The implementation of the algorithm and computer simulation of the virtual phantoms is given in Chapter 3 as well as the experimental scanning procedure of the physical phantoms. The results are presented and discussed in Chapter 4. A summary is given in Chapter 5.

CHAPTER 2

THEORY

2.1 Attenuation of Sound Waves

While an acoustic wave is traveling through a medium with a speed c , some of its energy will be dissipated. This effect is called *attenuation* of the sound wave. In many situations this energy dissipation is negligible for the distance of interest [8]. However, for most biological media the attenuation of the sound waves is rather large and cannot be neglected. For harmonic waves (waves with mono-frequency $\omega = 2\pi f$) the loss due to the medium can be described by the lossy Helmholtz equation

$$\nabla^2 \mathbf{p} + \mathbf{k}^2 \mathbf{p} = 0 \quad (2.1)$$

where \mathbf{p} is the acoustic pressure, and \mathbf{k} is the complex wave vector which describes the direction a wave is traveling. The complex wave vector can be expressed by

$$\mathbf{k} = k - j\alpha \quad (2.2)$$

where the real part of the complex wave vector (k) has the magnitude of ω/c and is equal to the wave vector of a wave traveling through a nonattenuating medium. The attenuation is described by the imaginary part of equation 2.2 and is denoted by α .

A solution of equation 2.1 for a plane wave traveling in the positive x direction is given by

$$\mathbf{p} = P_0 e^{-\alpha x} e^{j(\omega t - k_x x)} \quad (2.3)$$

where P_0 represents the pressure amplitude at an initial point $x_0 = 0$. The

intensity I of a plane harmonic wave can be calculated using

$$I = \frac{P^2}{2\rho c} \quad (2.4)$$

where P is the pressure amplitude of the wave and ρ_0 is the equilibrium density of the medium. Combining equation 2.4 and 2.3 gives

$$I(x) = \frac{(P_0 e^{-\alpha x})^2}{2\rho c} = I_0 e^{-2\alpha x} \quad (2.5)$$

where I_0 describes the initial intensity of the wave.

2.2 Attenuation Mechanism

In this section a brief overview of the attenuation mechanism is given. A more detailed description can be found in [1, 4, 8]. The total attenuation α of sound waves can be generally described by two effects: (1) those effects which are intrinsic to the medium and convert acoustic energy into thermal energy (α_{abs}) and (2) redirecting energy (scattering) due to boundaries of the medium (α_{scat}) [1, 4, 8]. Losses due to the medium are referred to as *absorption* and can be subdivided into *classical* and *molecular* absorption. The classical absorption includes viscous losses and losses due to thermal conductivity. Molecular absorption describes conversion of kinetic energy of molecules into (1) potential energy, (2) rotational and vibrational energy (polyatomic molecules), and (3) energies of association and dissociation between ions of different species and complex ionized solutions [8]. An overview of those attenuation mechanisms is given in Figure 2.1.

2.2.1 Sound Scattering

Scattering is a rather complicated process and depends strongly on frequency and the geometry of the scatterer. The loss due to scattering is caused by the redirection of acoustical energy out of the sound path. This energy will be lost since it will eventually be transferred into thermal energy by the absorption mechanism explained in section 2.2.2. Following is just a brief overview of some scattering models given.

Sound will be reflected at ultrasonic inhomogeneities, which are described by changes in the compressibility and density of the medium [2, 9–11]. If the inhomogeneities are comparable in size to the acoustic wavelength λ , then scattering takes place. Scattering will have directionality and depends on the shape and size of the scatterer. Rayleigh [12] developed the first model describing scattering of small structures such as spheres with radius a . For spheres the Rayleigh model is only valid when the radius is much smaller than the wavelength ($ka \ll 1$) [1, 12]. The scattered pressure in the far field has an f^2 frequency dependency and is proportional to a^3 . A scattering model for a fluid filled spheres was introduced by Anderson [10]. Faran developed a model for solid scatterers such as spheres and cylinders [11] incorporating shear waves into the derivations.

2.2.2 Classical Absorption

Classical absorption includes losses due to viscosity and thermal conductivity. Stokes developed the first theory of sound absorption by incorporating viscosity into the force equation. There are two kinds of viscosity: *shear* and *bulk*. The shear viscosity can be measured directly and describes the diffusion of the momentum between layers of fluids which possess different velocities [8]. The bulk viscosity cannot be measured directly and describes the energy losses when a fluid is compressed. The absorption due to shear and bulk viscosity is proportional to the square of the frequency [8].

Thermal conductivity is another mechanism that produces absorption. Kirchhoff included thermal conductivity to develop the so called classical absorption coefficient α_{clas} . When a sound wave travels through a fluid, compressed regions will have a higher temperature than rarefied regions. Therefore, molecules from the hotter regions have a higher kinetic energy and will diffuse into regions with lower temperature where they will collide with colder molecules and transfer some of their kinetic energy. This heat flow is irreversible, so the energy is lost.

2.2.3 Molecular Absorption

The classical absorption theory describes well the observed absorption of monoatomic gases. The internal structure of the molecules has to be taken into account in order to explain the observed values of absorption for polyatomic molecules [8]. Polyatomic gases have, in addition to the three translational degrees of freedom, rotational and vibrational internal states which can be populated. The transfer of energy from the translational state (kinetic energy) to the internal states (rotational and vibrational states) takes some time (τ) which is called relaxation time. If the period of the acoustic oscillation is long compared to the relaxation time ($\omega\tau \ll 1$), then the state can be fully populated, meaning energy can be transferred fast enough between translational states and internal states while the acoustic conditions are still the same (quasi stationary). If the acoustic period is much shorter than the relaxation time ($\omega\tau \gg 1$), then acoustic conditions will already be reversed before the internal states can be populated. Therefore, just small amounts of energy can be transferred into internal states, which leads to small losses as well. The energy loss will be maximized for periods close to the relaxation time ($\omega\tau \approx 1$). Therefore, the overall absorption will be dominated by the classical absorption for $\omega \gg 1/\tau$ and $\omega \ll 1/\tau$, but for $\omega \approx 1/\tau$ the molecular absorption will contribute significantly causing a peak in the overall absorption.

2.3 Attenuation in Biological Tissue

In the previous sections it has been shown that the attenuation (α) is a rather complex process and depends on the composition of the media, its temperature, ambient pressure and frequency. However, for biological soft tissue the temperature and ambient pressure can be assumed to be constant and therefore the attenuation coefficient can be described by a model which takes only frequency into account. A variety of experimental methods have been used to determine the attenuation-versus-frequency characteristics [1, 13, 14]. A good approximation for the frequency dependence of the attenuation for most soft tissue is given by

$$\alpha = \beta f^n \tag{2.6}$$

where β is the attenuation slope and n lies in the range of 1 to 2 for most soft tissues [1].

2.4 Estimation of Attenuation from Backscattered Sound

2.4.1 Received Voltage from a Single Scatterer

Most of the derivations are based on [5, 15]. The received voltage $V(f)$ of a single scatterer at the position $\vec{r} = [x, y, z]$ (see Figure 2.2) can be expressed as

$$V(f) = T_T(f) D(f, \vec{r}) U(f) D(f, \vec{r}) T_R(f) \quad (2.7)$$

where $T_T(f)$ and $T_R(f)$ are the electro-acoustic transfer functions for transmit and receive respectively, $D(f, \vec{r})$ is the diffraction transfer function, and $U(f)$ is the backscattered amplitude of the scatterer. In all the derivations a shock excitation (modeled by a Dirac pulse) of the transducer is assumed which translates into unity in the frequency domain. The diffraction transfer function $D(f, \vec{r})$ for a source with the aperture function $S(\vec{r}_s)$ can be expressed by using the Rayleigh-Sommerfeld equation

$$D(f, \vec{r}) = \int \int_{S_S} S(\vec{r}_s) \frac{1}{4\pi R} \exp(jkR) dS_S \quad (2.8)$$

where $R = |\vec{r} - \vec{r}_s|$ is the distance between source point and scatterer location. Using 2.2 for the wave number gives

$$D(f, \vec{r}) = \int \int_{S_S} S(\vec{r}_s) \frac{1}{4\pi R} \exp(jkR) \exp(-\alpha R) dS_S. \quad (2.9)$$

If the scatterer is far away from the radiating aperture then the distance between source and observation point can be approximated by the axial distance z ($R \approx z$). Therefore, the attenuation and diffraction can be separated [15]:

$$D(f, \vec{r}) \approx \exp(-\alpha z) \int \int_{S_S} S(\vec{r}_s) \frac{1}{4\pi R} \exp(jkR) dS_S = \exp(-\alpha z) D_0(f, \vec{r}). \quad (2.10)$$

Therefore, equation 2.7 can be expressed as

$$V(f) = T_T(f) D_0(f, \vec{r}) U(f) D_0(f, \vec{r}) T_R(f) \exp(-2\alpha z). \quad (2.11)$$

2.4.2 Received Voltage from Tissue

One approach of modeling biological tissue is to describe it by a continuous distribution of scatterers [15]. Then each differential volume element dV radiates a spherical wave with a scattering amplitude of $U(f, \vec{r})$. Assuming that the frequency dependency of the scattering coefficient ($SC(f, \vec{r})$) is independent of the location of the scatterer ($SC(f, \vec{r}) = U(f) s(\vec{r})$) then the received voltage from such a medium can be obtained by integrating throughout the scattering region V

$$V(f) = T_T(f) U(f) T_R(f) \int \int \int_V D^2(f, \vec{r}) s(\vec{r}) dV. \quad (2.12)$$

The attenuation slope can be evaluated by considering only scatterers located within a small slice with a cross sectional area S and a thickness dz (Figure 2.3). If the speed of sound is assumed to be constant then the backscattered voltage at a distance $d = c\tau/2$ can be obtained by truncating the received RF line at the time (τ) by a window function (w). However, for infinitesimally small window sizes, $w \rightarrow \delta$, the window function will approach a Kronecker delta pulse $\delta(R)$ and only scatterers at the distance d will contribute to the received echo if a plane wave is assumed. Therefore, equation 2.12 can then be rewritten as

$$V(f, d) = T_T(f) U(f) T_R(f) \int \int \int_V D^2(f, \vec{r}) s(\vec{r}) \delta(R - d) dV. \quad (2.13)$$

The field of a piston source can be rather complicated (near field) and therefore the shape of the iso-distant surface is more complex than indicated in Figure 2.3. However, for the focal region of a focused source a plane wave approximation is valid. The spatial scattering amplitude $s(\vec{r})$ can be represented by its average value \bar{s} assuming a uniform distribution

leading to

$$E[V(f, d)] = T_T(f) U(f) T_R(f) \left\langle \int \int \int_V D^2(f, \vec{r}) s(\vec{r}) \delta(R - d) dV \right\rangle \quad (2.14)$$

where $E[\cdot]$ denotes the expected value. Separating the diffraction and attenuation in a similar fashion to equation 2.10 yields

$$E[V(f, d)] = T_T(f) U(f) T_R(f) \exp(-\alpha d) H_0^2(f, \vec{r}) \quad (2.15)$$

where

$$H_0(f, \vec{r}) = \bar{s} \int \int \int_V D_0(f, \vec{r}) \delta(R - d) dV \quad (2.16)$$

as the transfer function of the lossless scattering medium.

2.4.3 Diffraction Correction

The reflected signal of a planar reflector can be used for diffraction correction [16]. The received power ($P_S(f, d)$) from an unknown sample of a scattering medium can be expressed by using equation 2.15. Rewriting 2.15 gives

$$E[P_S(f, d)] = [|T_T(f) U_S(f) T_R(f) H_0^2(f, \vec{r}) \exp(-\alpha_S d)|]^2 \quad (2.17)$$

where the subscript s denotes the sample measurement. One way to correct for the system dependent parameters such as $T_T(f)$, $T_R(f)$, and $H_0(f, \vec{r})$ is to perform a reference measurement with the same system settings. This can be done by moving a planar reflector axially with incremental steps through the transducer field and acquiring the system response at every distance d (Figure 2.4). The received power from such a reference measurement performed in a medium with negligible attenuation can be written as

$$E[P_{Ref}(f, d)] = [|T_T(f) U_{Ref}(f) T_R(f) H_0^2(f, \vec{r})|]^2 \quad (2.18)$$

where the subscript *Ref* denotes the reference measurement. A correction for diffraction may be performed by dividing 2.17 by 2.18, that is,

$$R(f, d) = \frac{E[P_S(f, d)]}{E[P_{Ref}(f, d)]} = \left[\left| \frac{U_S(f)}{U_{Ref}(f)} \exp(-\alpha_S d) \right| \right]^2. \quad (2.19)$$

This spectral ratio has no instrumentation dependent factors and is only defined by properties of the medium.

2.4.4 Attenuation Slope Estimation

The attenuation slope β can be estimated by measuring the downshift of the center frequency of a pulse. A method assuming a Gaussian shaped pulse and linear frequency dependency of the attenuation ($n = 1$ in equation 2.6) was introduced by R. Kuc et al. [7]. In order to estimate the attenuation of a medium correctly, diffraction of the transducer must either be negligible or corrected for. One way of obtaining the desired pulse with no diffraction ($P_{Cor} = [|V_{Cor}|]^2$) is to filter the spectral ratio, $R(f, d)$ (equation 2.19), with a Gaussian filter [6, 7, 15]. However, the wavefront at the focus of a source is planar so that the echo obtained from the focus can be described by the transducer pulse-echo transfer function $V(f, d_F) = T(f) = T_T(f) T_R(f)$. Since the transducer transfer function can be approximated by a Gaussian function, the spectral ratio is filtered with $V(f, d_F)$

$$P_{Cor}(f, d) = \left[\left| \frac{U_S(f)}{U_{Ref}(f)} V(f, d_F) \right| \right]^2 \exp(-2\alpha_S d) \quad (2.20)$$

where d_F denotes twice the distance from the radiating aperture to the focus. Substituting the round trip distance d by $z_0 = z - d/2$ and approximating the squared bracketed term of equation 2.20 by a Gaussian function ($\exp\left[\frac{-(f-f_0)^2}{2\sigma^2}\right]$) gives

$$P_{Cor}(f, z_0) = \left[\left| \frac{U_S(f)}{U_{Ref}(f)} V(f, d_F) \right| \right]^2 \exp(-4\alpha_S z) \approx \exp\left(\frac{-(f-f_0)^2}{2\sigma^2} - 4\alpha_S z_0\right) \quad (2.21)$$

where f_0 denotes the center frequency of the pulse, and σ is the pulse width. Assuming linear frequency dependency for the attenuation ($\alpha = \beta f$) gives

$$P_{Cor}(f, z_0) = A_\alpha \exp\left(\frac{-(f - f_\alpha)^2}{2\sigma^2}\right) \quad (2.22)$$

with

$$f_\alpha = f_0 - 4\beta\sigma^2 z_0 \quad (2.23)$$

and

$$A_\alpha = \exp\left(\frac{f_0^2 - f_\alpha^2}{2\sigma^2}\right). \quad (2.24)$$

From equation 2.22 it can be seen that the pulse shape remains Gaussian but its amplitude decays exponentially (equation 2.24) and the center frequency of the pulse shifts to lower frequencies (equation 2.23). A complete derivation of equation 2.22 is given in appendix A.1. The attenuation slope β can be estimated by measuring the downshift of the center frequency (f_α) with depth. The rate of downshift can be obtained by taking the derivative of f_α with respect to z_0

$$\partial f_\alpha = -4\beta\sigma^2 \partial z_0. \quad (2.25)$$

The attenuation slope can be obtained by

$$\beta = -\frac{1}{4\sigma^2} \frac{\partial f_\alpha}{\partial z_0}. \quad (2.26)$$

This is the fundamental equation which is used to estimate the local attenuation slope of the medium.

Rewriting equation 2.25 and noting that the pulse length (PL) of a Gaussian pulse is inversely proportional to the absolute bandwidth ($\sigma \propto \frac{1}{PL}$) gives

$$\partial f_\alpha \propto \sigma^2 \partial z_0 \propto \frac{\sigma}{PL} \partial z_0. \quad (2.27)$$

When the change in z_0 is normalized by the pulse length ($\partial z_0 = \gamma PL$), equation 2.27 can be rewritten as

$$\partial f_\alpha \propto \frac{\sigma \gamma PL}{PL} \propto \sigma. \quad (2.28)$$

Equation 2.28 shows that the amount of downshift for a Gaussian pulse is proportional to the absolute bandwidth when ∂z_0 is normalized to the pulse length. Another interesting aspect is that the change of the center frequency per unit depth will be proportional to the absolute bandwidth if ∂z_0 is normalized by PL :

$$\frac{\partial f_\alpha}{\partial z_0} \propto \frac{\partial f_\alpha}{\gamma PL} \propto \frac{\sigma}{PL} \propto \sigma. \quad (2.29)$$

2.5 Simulation of an Attenuating Medium

The simulations are based on [17]. The received voltage for a single scatterer located at a depth z ($|\vec{r}| \approx z$) with no diffraction ($D_0(f, \vec{r}) = 1$) and a scattering amplitude of unity ($U(f)$) can be expressed based on 2.11 as

$$V(f) = T_T(f) T_R(f) \exp(-2\alpha z) = G(f) A(f, z). \quad (2.30)$$

Generally the attenuation term $A(f, z)$ can be modeled as a filter with an amplitude and phase. Assuming linear frequency dependency of the attenuation, the magnitude of $A(f, z)$ can be written as

$$|A(f, z)| = 10^{\frac{-\beta_{dB} f^2 z}{20}} \quad (2.31)$$

where β_{dB} denotes the attenuation slope in dB/cm-MHz whereas f is expressed in MHz and z in cm.

Each harmonic of the excitation pulse $G(f)$ has to travel the distance $2z$. This corresponds to a delay $t_0 = 2z/c$ which can be achieved by considering the Fourier-Transform property

$$H(\omega) e^{-j\omega k} \Leftrightarrow h(t - k) \quad (2.32)$$

where $H(\omega)$ is the Fourier transform of $h(t)$. Therefore, the attenuation corresponds to a filter with linear phase

$$A(f, z) = |A(f, z)| e^{j2\pi f \frac{2z}{c}}. \quad (2.33)$$

However, Kuc [17] showed that for a linearly attenuating medium (Plexiglas) the use of a minimum phase filter gives better agreement of the

simulated RF data with experimental data. A minimum phase can be obtained using the Hilbert-Transform pair

$$\angle A(f, z) = \frac{1}{2\pi} \mathbf{P} \int_{-\pi}^{\pi} \log [|A(\phi, z)|] \cot \left(\frac{\phi - \omega}{2} \right) d\phi \quad (2.34)$$

where \mathbf{P} denotes the Cauchy principle value. The total phase of the attenuation filter can then be written as the summation of the linear ($\angle A_{lin}(f, z)$) and minimum phase ($\angle A_{min}(f, z)$) term

$$\angle A(f, z) = \angle A_{lin}(f, z) + \angle A_{min}(f, z). \quad (2.35)$$

Therefore, the received voltage from a single scatterer at a depth z can be expressed by

$$v(t) = F^{-1} \{G(f) |A(f, z)| \angle A(f, z)\} \quad (2.36)$$

where F^{-1} denotes the inverse Fourier transform. For a collection of N scatterers the echoes will superimpose and equation 2.36 can be rewritten as

$$v(t) = F^{-1} \left\{ \sum_{n=1}^N G(f) |A(f, z_n)| \angle A(f, z_n) \right\} \quad (2.37)$$

where the linear property of the Fourier transformation is used. This equation was used for calculating all RF data from the virtual phantoms.

2.6 Figures

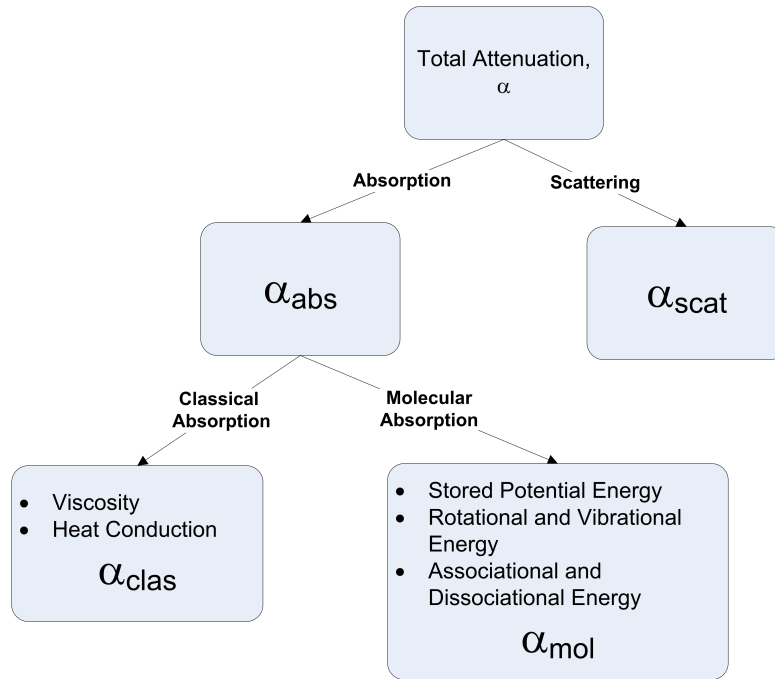


Figure 2.1: Schematic representation of the effects contributing to the attenuation of a sound wave.

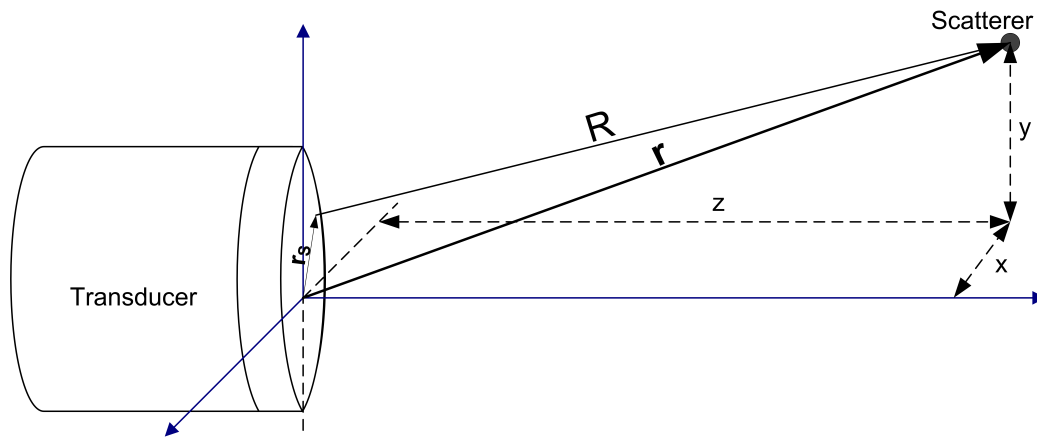


Figure 2.2: Layout of a single scatterer.

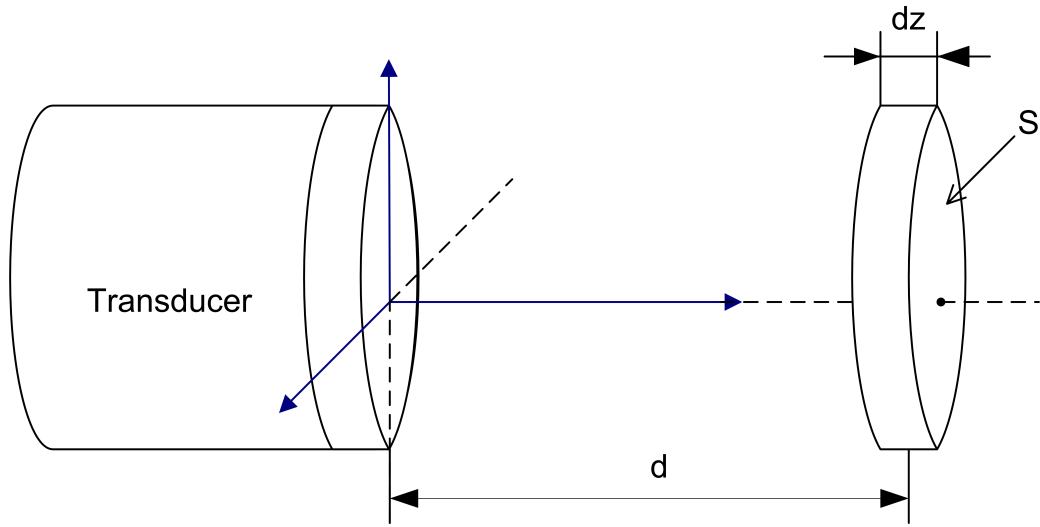


Figure 2.3: Geometry of an infinitesimally thin slice containing the scatterers that will contribute to the pulse/echo response at the time $\tau = 2d/c$.

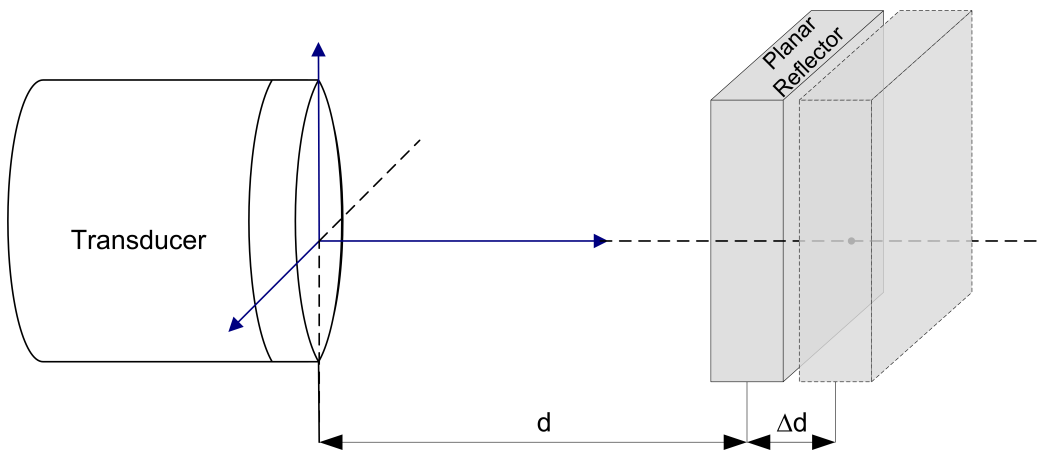


Figure 2.4: Schematic of procedure for acquiring the reference data for a ultrasonic system. A planar reflector is axially moved through the transducer field and at each depth d the system response is acquired.

CHAPTER 3

METHODOLOGY

3.1 Simulated RF Data

All virtual phantoms were created based on equation 2.37. A MatlabTM(The MathWorks Inc., Natick, MA) program was written whose structure is shown in Figure 3.1. In the simulations the beam had a rectangular cross section (1×1 mm) which insonified a volume of uniformly distributed scatterers (see Figure 3.2). For the round trip transducer transfer function ($G(f)$) a Gaussian pulse was used with center frequency f_0 , and a fractional bandwidth (BW) corresponding to the -3 dB fall off. A derivation of how the fractional bandwidth relates to σ is shown in section A.2. The scatterer density was 15 scatterers per resolution cell for all virtual phantoms. The volume of the resolution cell was defined as the cross section of the beam multiplied by the -60 dB pulse length. The round trip transfer function of an individual scatterer was obtained by first computing the distance from the center of the aperture to scatterer location. Afterwards, the magnitude ($|A(f, z)|$) of the attenuation filter was calculated using equation 2.31. The phase of the filter consists of two parts $\angle A_{lin}(f, z)$ and $\angle A_{min}(f, z)$. The minimum phase part, $\angle A_{min}(f, z)$, is calculated using the phase of equation 2.34 and the linear part, $\angle A_{lin}(f, z)$, of the phase is calculated using equation 2.33. The simulated RF lines were obtained by computing all round trip transfer functions of each individual scatterer located within the beam volume and performing a cumulative summation of the round trip transfer functions from all individual scatterers. The inverse Fourier transform of the cumulative summation of all scatterers within the beam will give the final RF line (equation 2.37).

Three sets of virtual phantoms were created which had attenuation slopes of 0.5, 1.0 and 1.5 dB/cm-MHz. From each of the virtual phantoms,

Table 3.1: Properties Used to Generate the RF Data

AS (dB/cm-MHz)	0.5		1.0		1.5	
f_0 (MHz)	f_{min}	f_{max}	f_{min}	f_{max}	f_{min}	f_{max}
$BW_{min} = 20$ (%)	12	22	6	14	4	8
$BW_{max} = 65$ (%)	12	22	6	14	4	8

RF data sets consisting of 600 uncorrelated RF lines were computed for a variety of different center frequencies (f_0) and fractional bandwidths (BW). The maximum penetration depth for each RF data set was chosen to limit the downshift in center frequency of the pulse to half of the absolute bandwidth ($BW f_0/2$). Therefore, the maximum depth of the virtual phantoms can be described by rearranging equation 2.25.

$$\partial z_0 = \frac{BW f_0}{8\sigma^2\beta}. \quad (3.1)$$

In order to keep the memory requirements of the computations reasonable, the maximum penetration depth was limited to 50 mm yielding a vector with length less than 8192 points for a sampling frequency of 100 MHz. The resulting center frequencies and bandwidths for the three different phantoms are shown in Table 3.1. Each RF data set was generated 10 times to obtain the average and variance of the estimates. The code was optimized for speed by vectorizing the summation in equation 2.37. The computations of the different RF data sets were run in parallel on a cluster using four eight-core nodes. The computational time for one RF data set (600 RF lines) was approximately 5 min.

3.2 Physical Phantoms

Physical phantoms are simplified models of biological tissue. Phantoms have the advantage that their properties, such as scattering and attenuation, can be well controlled. Scattering depends on the scatterer properties, such as shape, size and density. There are several theoretical models of scattering from simple geometries. For instance, the scattering of a fluid sphere due to an incident plane wave can be theoretically described using the Anderson model [10]. Faran [11] introduced a theory which

Table 3.2: Physical Phantom Properties

Property	Pantom	
	A	B
Scatterer	Glass Beads	Glass Beads
Background Material	Agarose/ n-propanol/ milk/ H_2O	Agarose/ n-propanol/ milk/ H_2O
Scatterer Diameter	75-90 μm	9-43 μm
Scatterer Concentration	5/ mm^3	800/ mm^3
Measured AS (dB/cm-MHz)	0.46	0.68

describes the scattering from solid cylinders and spheres integrating shear waves into the model. The resulting attenuation also depends on the background material and can be altered by combining different materials.

All experiments were performed using two physical phantoms referred to as *A* and *B* [18]. These phantoms were made of a gelatin milk mixture in which glass beads were embedded. While still hot, the liquid mixture was poured into Acrylic cylinders which were sealed on top and bottom with Saran wrap. The cylinders were rotated while the mixture cooled so that a uniform distribution of the glass beads was maintained. The Saran wrap “lids” serve as *acoustic windows* with a frequency dependent transmission coefficient [18]. A sketch of the physical phantoms is shown in Figure 3.3. The properties of the phantoms are shown in Table 3.2.

The attenuation obtained from broadband insertion loss measurement was taken as the true measure of the attenuation [13]. This measurement was performed using a 7.5 MHz nominal center frequency single-element transducer and the average of three independent experiments is summarized in Table 3.3.

3.3 RF data Acquisition Physical Phantoms

The layout of the experimental setup to scan the physical phantoms is shown in Figure 3.4. Both phantom A and B were scanned with two single element transducers (Model V380 and V321, Panametrics Inc., Waltham, MA) with a nominal center frequency of 3.5 and 7.5 MHz. The transducers were characterized using a wire technique to obtain the true field as well as

the true center frequency and bandwidth [19]. The measured values are shown in Table 3.3. The transducers were mounted into a micro-precision positioning system (Daedal Inc., Harrison City, PA) which is controlled by a personal computer. The transducers were shock excited using a pulser/receiver (Model 5900, Panametrics Inc., Waltham, MA) and the output signal was digitized with a 14-bit A/D card (Model PDA 14, Signatec Inc., Newport Beach, CA) which operated with a sampling frequency of 200 MHz. All scans were conducted in a tank filled with degassed water.

First, a reference scan from a planar Plexiglas surface was acquired by placing the Plexiglas perpendicular to the transducer beam. The transducer was positioned towards the Plexiglas surface yielding a maximum receive amplitude. The power spectrum of the received reflection was evaluated for any nonlinear distortions, such as harmonics and subharmonics. The settings of the pulser were adjusted in order to achieve a non-distorted transducer response. Reference data was acquired by moving the transducer axially and recording the reflections from the Plexiglas surface at half-wavelength intervals through the entire depth of field of the transducer. The phantoms were scanned by placing the focus 10 mm underneath the surface of the phantom. The transducer was translated laterally with a 1.5 mm step size between each scan point yielding uncorrelated RF lines (see Figure 3.4). At each scan point the time average of 200 pulses was recorded. A total of 512 RF lines was acquired per phantom.

Table 3.3: Properties of the Single Element Transducers

Transducer	3.5	7.5
f_0 (MHz)	3.9	8.2
BW (%)	44	36
-6 dB Beamwidth (μm)	8180	3990
-6 dB DOF (mm)	31.9	16.7

3.4 Attenuation Slope Estimation

The attenuation slope estimation scheme is based on equation 2.25. The estimation program was written in Matlab. The estimation algorithm is

outlined in Figure 3.5. The RF data obtained by simulations or by actual ultrasonic scans is read into the program. A region of interest (ROI) is selected either manually by the user or from a previously saved ROI. The ROI is then segmented into sections based on predefined settings for the lateral and axial section length (l_{lat} and l_{axi}) and the lateral and axial overlap between sections (O_{lat} and O_{axi}) (see Figure 3.6). The focus of the transducer was defined as the transducer-to-Plexiglas distance that yielded the maximum signal amplitude. The depth of field of the transducer was defined as the axial length where the maximum reference signal drops to 50 percent of the signal magnitude of the focus.

An average power spectrum (PS_{samp}) is computed for each section. Reference power spectra (PS_{ref}) are computed for the individual depths of each section for purposes of diffraction correction. The reference scan data contained several reflections corresponding to the depths of each section, which were used to compute an average reference power spectrum. On the right-hand side of Figure 3.5 the attenuation slope estimation scheme is shown. The corrected spectra (PS_{Cor}) is computed by means of equation 2.21. The analysis bandwidth is obtained by a user defined threshold which typically ranged from 8 to 15 dB from the peak of the corrected spectrum. The estimated center frequencies (f_{α}) and bandwidths (σ) were obtained by fitting a second order polynomial to each PS_{Cor} in the logarithmic domain. It has been shown, that using the logarithmic domain yielded more accurate estimates of the center frequency than fitting a Gaussian function in the linear domain. The rate of the downshift of the center frequency vs. depth is obtained by a linear regression of the values of f_{α} versus the section depths. The attenuation slope is calculated using equation 2.25.

3.5 Figures

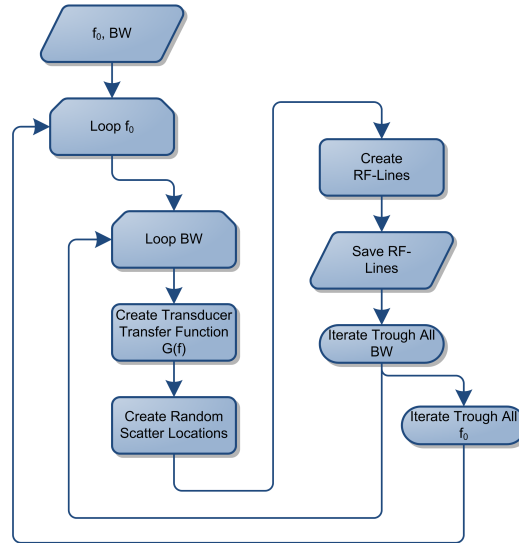


Figure 3.1: Flow chart of the program code which generates the virtual phantoms. In the first block two vectors containing all center frequencies (f_0) and fractional bandwidths (BW) of interest are created. Second, the transducer transfer function ($G(f)$) is calculated for each center frequency and fractional bandwidth. A Gaussian shaped filter with a -3 dB fractional bandwidth was used for the transducer transfer function. In the third block, the random scatterer locations are calculated using a normal distribution. Fourth, for each scatterer the round trip transfer function ($A(f, z)$) is calculated using a minimum phase filter. The RF line is created by superimposing the impulse responses of all scatterers.

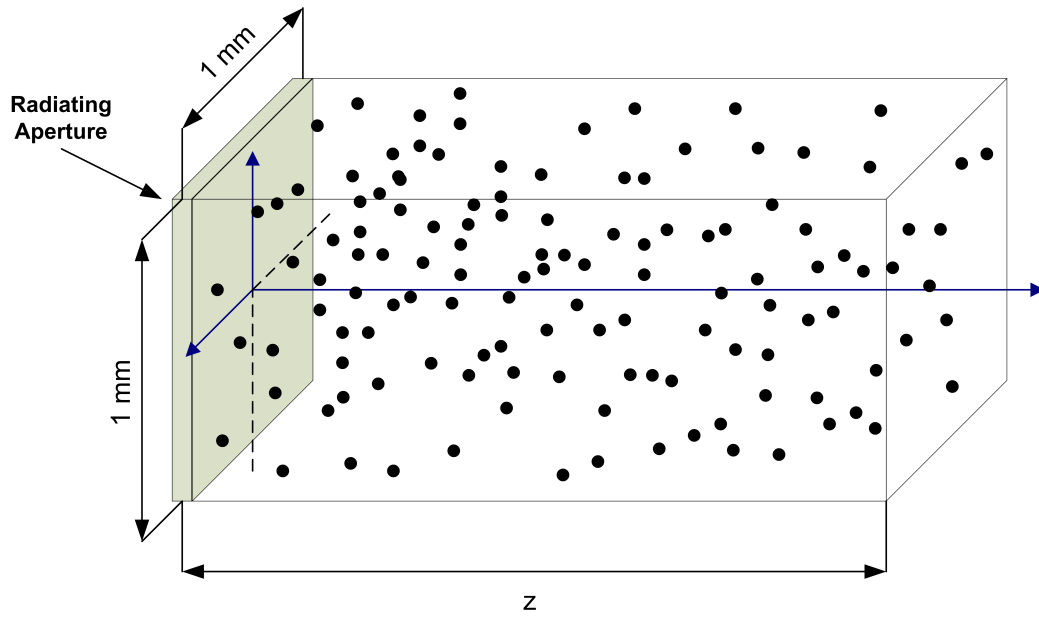


Figure 3.2: Geometry of the transducer model used for the virtual phantoms.

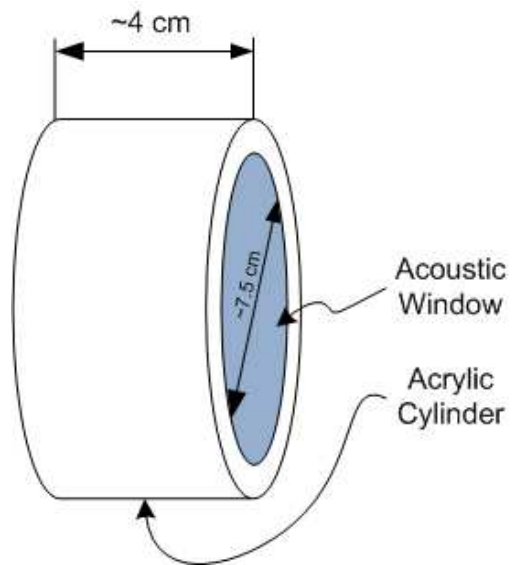


Figure 3.3: Geometry of physical phantoms.

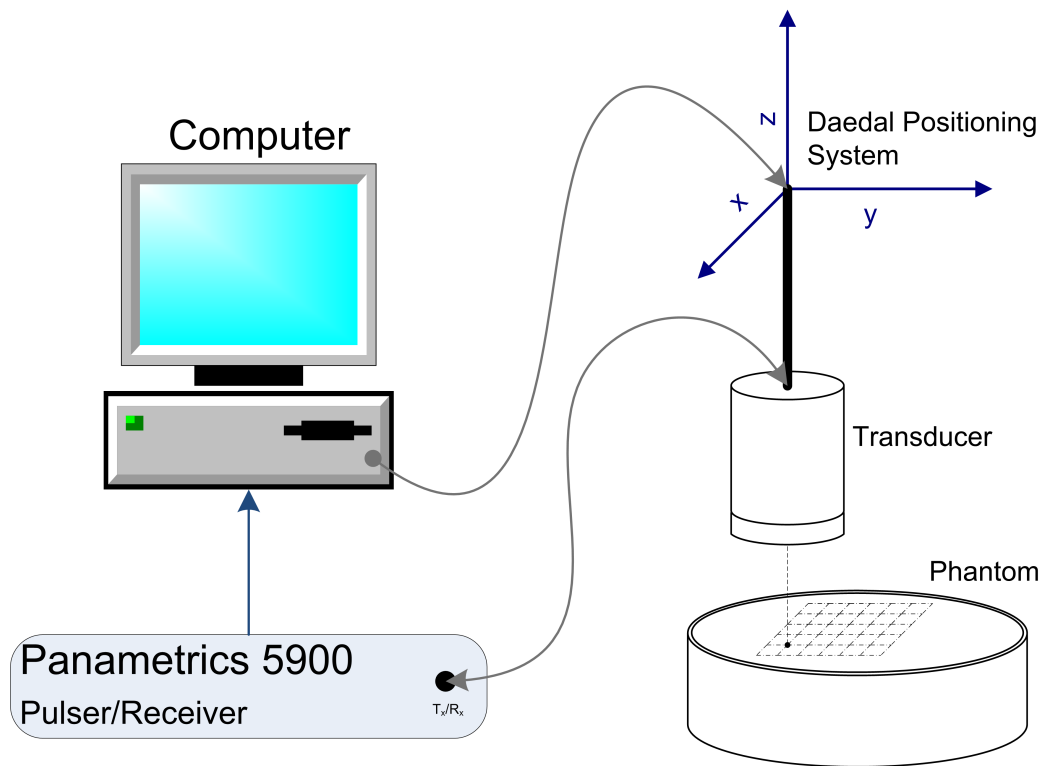


Figure 3.4: Layout of the experiment to acquire the RF data from the physical phantoms.

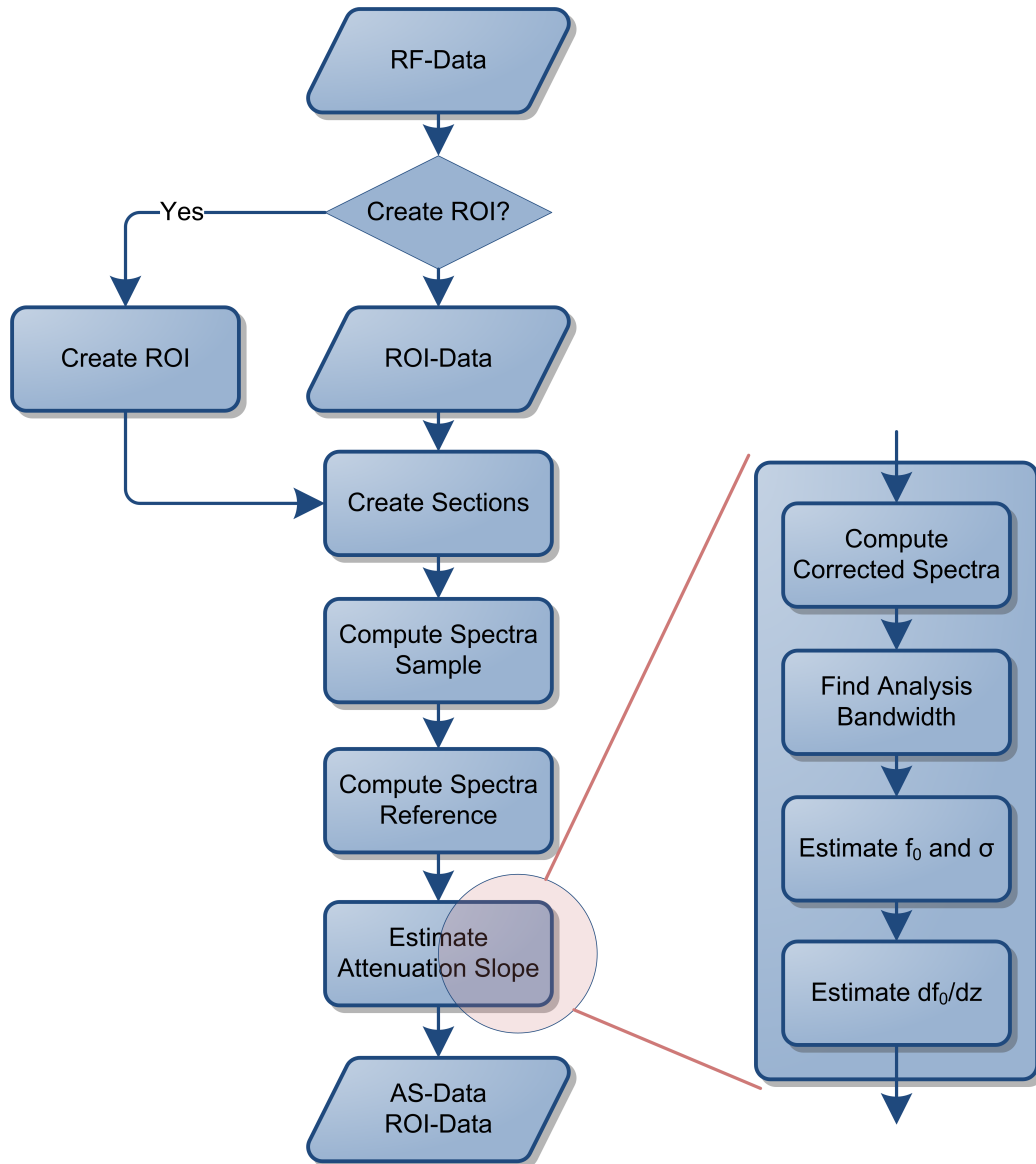


Figure 3.5: Flow chart of the attenuation slope estimator code. Each block represents a function within the estimator code. On the right-hand side the attenuation slope estimation procedure is shown in detail.

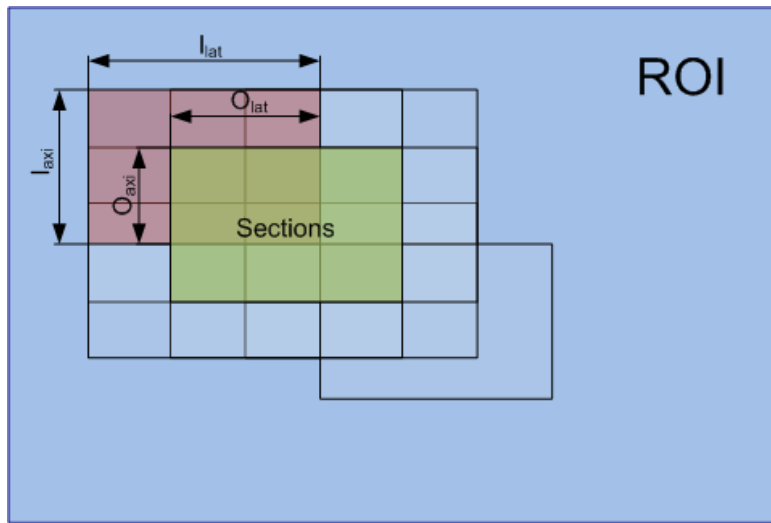


Figure 3.6: Geometry of the section within the ROI. Note that for clarity not all sections were drawn into the ROI.

CHAPTER 4

RESULTS AND DISCUSSION

4.1 Accuracy of the Gaussian Fit

4.1.1 Estimation Performance for a Single Scatterer without Attenuation

As described in section 2.4.4 the attenuation slope can be estimated by measuring the downshift of a pulse's center frequency with depth. The center frequency of the pulse was detected by fitting a quadratic function to power spectra in the logarithmic domain. The accuracy of the fit may depend on the total bandwidth of the Gaussian pulses as well as on the analysis bandwidth used. The same Gaussian pulses used in the simulations were created and had a center frequency and relative bandwidth (BW) ranging from 4 to 22 MHz and 20% to 65% respectively. The Fourier transformations of the pulses were computed and the center frequency (f_0) and absolute bandwidth (σ) were estimated. The estimation results for f_0 and σ using a -6 dB analysis bandwidth are shown in Figures 4.1 and 4.2. The color bar shows the absolute error in percent.

In Figures 4.1 and 4.2 it can be seen that the absolute error of the f_0 and σ estimates stays well below 0.012 and 0.28 percent, respectively, for all tested combinations of f_0 and BW . It can be seen that the error is relatively constant for the different f_0 but increases with increasing BW . Figure 4.1 shows that the error of the f_0 estimates is significantly higher for fractional bandwidths of 65 percent. Looking at the error as a function of bandwidth (Figure 4.3) shows that the error starts to increase for fractional bandwidths greater than 50%. At this point a quarter of the power of the pulse will be at negative frequencies, which may introduce a bias toward lower frequencies. It also can be seen that this effect is more pronounced for

lower analysis bandwidths (see Figure 4.3). Similar effects can be seen for the total bandwidth σ (Figure 4.4).

The influence of the analysis bandwidth of the error of f_0 and σ is shown in Figure 4.5. It can be seen that the analysis bandwidth has a relatively low influence on the error over the range tested but still alters the estimates of the pulses with a high fractional bandwidth (note the dimensions of the y-axis).

4.1.2 Estimation Performance for a Single Scatterer in an Attenuating Medium

The accuracy of the fit may also depend on the amplitude of the power spectrum, which will change when the pulse is propagating in an attenuating medium. In order to model the influence of the decaying amplitude, Gaussian pulses were generated with a center frequency and relative bandwidth (BW) ranging from 4 to 8 MHz and 20% to 65%, respectively. The power spectra of the pulses ($|G(f)|^2$) were multiplied by an attenuation term $\exp(-4z\beta f)$ where z denotes the depth, which was normalized to the pulse length PL . The analysis bandwidth corresponded to -6 dB. The estimated errors for f_0 are shown in Figure 4.6. The error of the absolute bandwidth is shown in Figure 4.7.

The error of the f_0 estimates is clearly higher for pulses which propagated through an attenuating medium. The error in f_0 for 4 and 8 MHz is shown in Figure 4.8. The error increases at a higher rate for pulses with a higher fractional bandwidth. There is no apparent dependence of the error on the center frequency. This may suggest that the estimation performance of the center frequency is correlated to the fractional bandwidth. This statement is supported by the fact that, for Gaussian pulses propagating in a medium with linear frequency dependency, the absolute bandwidth σ stays constant (no dispersion) but the center frequency shifts to lower values with depth. Therefore, the fractional bandwidth has to increase in order to maintain a constant absolute bandwidth. This would also explain the steeper slope of the error for the high bandwidth pulses, since these pulses have a larger downshift per unit length than narrower pulses.

The error of the absolute bandwidth starts to increase rapidly only for

pulses with fractional bandwidths larger than 60%. Figure 4.9 shows the error of the σ estimates for pulses with a center frequency of 4 and 8 MHz. The error does not significantly depend on the center frequency but has a strong dependence on the fractional bandwidth. Looking at the error of σ for a larger range of BW (up to 95%) and depths (up to 200 PL) shows that the error of the σ estimates reaches a maximum and decreases afterwards toward negative values (see Figure 4.10). The peak of the 80% pulse occurs approximately at 85 PL . At this distance the center frequency of the pulse will be downshifted to approximately 3.24 MHz, which will translate to a fractional bandwidth of approximately 100%. This suggests that the error of the σ estimate is biased toward positive values for BW between 50% and 100%, whereas the bias becomes negative for BW greater than 100%.

4.2 Estimation Performance for a Distribution of Scatterers in an Attenuating Medium

In order to obtain a power spectrum from the backscattered signal obtained from a medium with randomly distributed scatterers, the RF lines need to be truncated by a window function centered at the depth of interest (see equation 2.13). The influence of the window length, also referred to as gate length or section length, on the estimation performance of f_0 and σ was tested by truncating the RF signal at a depth of 30 pulse lengths, corresponding to the middle of a rectangular window, for window sizes ranging from 1 to 20 pulse lengths. The average power spectrum of 6000 RF lines was computed so that the spatial variation noise was kept low. The error of f_0 and σ was estimated for f_0 , BW , and for several analysis bandwidths ranging from 4 to 8 MHz, 20% to 65%, and -1.5 to 12 dB respectively. The attenuation slope for the medium was 1.5 dB/cm-MHz. The error of the f_0 estimates for different window lengths is shown in Figures 4.11, 4.12, and 4.13 for analysis bandwidths corresponding to -1.5, -3.0, and -12.0 dB respectively.

The error of the σ estimation for window lengths of 1, 5, 10, and 15 pulse lengths is shown in Figures 4.14, 4.15, and 4.16 for analysis bandwidths relative to -1.5, -3.0, and -12.0 dB respectively.

In Figure 4.11 it can be seen that for increasing window lengths the error of f_0 increases more or less for all center frequencies and fractional bandwidths. Figure 4.17 shows this trend more clearly. This bias can be explained by considering that within the gate the signal will be altered due to attenuation. The signal from the beginning of the gate will have high frequency content with higher amplitudes than the signal from the end of the gate. Therefore, the power spectrum obtained from the gate will be biased toward higher frequencies depending on the gate length. As stated in equation 2.13, the optimal gating function would be a Dirac delta distribution. However, in practice this can only be approximated by small gate lengths.

In contrast, gating the signal with windows too short will introduce spectral broadening (see Figure 4.18). This effect can be seen for the σ estimates which were obtained using a 1 pulse length gating window (see Figures 4.14, 4.15, and 4.16). Figure 4.19 shows the error function of the σ estimates more clearly. Comparing the effects of the short gate lengths for the power spectra of two different fractional bandwidths (20% and 65%) shows that the relative amount of spectral broadening is the same (Figure 4.18). However, it can be seen that the slope of the Gaussian pulse with a 65% fractional bandwidth increases toward positive values around 1 MHz (right-hand side of Figure 4.18). This effect is due to the exponential character of the attenuation term which approaches unity for a frequency of zero. If the threshold of the analysis bandwidth is chosen too low, then this effect will introduce a bias for high BW pulses. This effect can be observed by looking at Figures 4.11 to 4.13 where the threshold of the analysis bandwidth is changed from -1.5 to -12 dB. In Figure 4.20 it can be seen that, for a -3 dB threshold for the analysis bandwidth, the estimates are not affected for windows with a length greater than 5 PL .

4.3 Spatial Variation Noise

The power spectrum obtained from a medium with randomly distributed scatterers will suffer from spatial variation noise and therefore the estimates of f_0 and σ will suffer. Averaging the power spectra from several uncorrelated RF lines will reduce this noise. In Figures 4.21 and 4.22 the

error of the f_0 estimates is shown, obtained from average power spectra using 27, 103, 201, and 608 RF lines. The results using gate lengths of 1 and 5 PL are shown in Figure 4.21 and 4.22, respectively.

From Figures 4.21 and 4.22 it can be seen that the error in the f_0 estimates decreases and settles around zero when a large number of RF lines are averaged. In Figure 4.23 the error in f_0 vs. number of RF lines is shown for different gatelengths (1, 3, 5, and 10 PL). From the plots it can be seen that shorter gate lengths seem to have less variation in the error of f_0 . Furthermore it seems that the absolute bandwidth has a major influence on the variance of the f_0 error since the observed fluctuations on the error are larger for the 8 MHz pulses.

In order to investigate this effect, the power spectra of a 4 MHz pulse with 20% and 65% fractional bandwidths were computed for gate lengths of 1, 5, and 10 PL and for 4, 15, 54, and 200 RF lines (Figures 4.24 to 4.29). Gate lengths of 1 PL produce a broader spectrum but the spatial variation noise is smoothed out. The windowing function can be thought of as a “filter” for the frequency domain signals. The Fourier transform of a rectangle is a *sinc* function which is convolved with the original “noisy” spectrum. This will “filter” or smooth out the noisy portion of the spectrum. This approach will work for all symmetric pulses. The filtering effect is reduced for larger gate lengths and less prominent for large bandwidth pulses. The displayed error is in some cases higher for shorter gate lengths but this may be due to the random character of the spatial variation noise and would need to be further investigated.

In Figure 4.30 the error of the σ estimates is shown. The estimates of the short gate length (1 and 23 PL) have a bias due to spectral broadening but the variation of the error seems to be low. The bias of the σ estimates is reduced for the longer gate lengths but the estimates for high bandwidth pulses seem to have higher variations.

4.4 Attenuation Slope Estimates

The attenuation slope can be estimated using equation 2.26. The attenuation slope is proportional to the amount the center frequency shifts down per unit length (df_α/dz) and inversely proportional to the square of

the absolute bandwidth σ . In Figure 4.31 the df_α/dz estimates are shown for a medium with 1.5 dB/cm-MHz attenuation slope. The df_α/dz estimates were obtained from five average power spectra which were computed from blocks with a width of 600 RF lines and a gate length of 10 PL . The region of interest had a total length of 50 PL . Figure 4.31 shows the average value obtained from 10 f_0 estimates. The theoretical shift, shown in Figure 4.32, was calculated using equation 2.23 and agrees well with the estimated values. The absolute value of the error of the f_0 estimates is shown in Figure 4.33. The error of the attenuation slope estimates, which was derived using the σ and f_0 estimates, is shown in Figure 4.34.

From Figure 4.33 it can be seen that the error in df/dz estimates does not decrease with increasing absolute bandwidth. The error seems rather to be randomly distributed among the different pulses. Looking at the error of the different pulses as a function of σ for different axial regions of interest ranging from 15 to 50 PL shows that the estimator is unbiased for all analysis depths (see Figure 4.35). The estimated error was obtained from 100 samples, each having a lateral extent of 60 RF lines. The slope (df/dz) was obtained from five gated regions which were distributed evenly within the analysis depth. The gate length for all estimates was 10 PL . In Figure 4.36 the variance of the df/dz estimates is shown for different analysis depths. The variance decreases with depth by about 35%. This is expected since the amount of downshift will increase with depth. The variance stays relatively constant for increasing σ . It was expected that the variance would decrease with increasing σ , since higher values of σ would cause higher shifts of the center frequency. As indicated in section 4.3 the variation of the error is higher for pulses with a large absolute bandwidth (Figure 4.23). This may suggest that the actual decreasing variance for higher bandwidth pulses is overlaid by an increasing variance introduced by the estimator. Figure 4.37 shows the variance of the f_0 estimates from the section at the largest depth (center of gate at 50 PL). It can be seen that the variance is higher for estimates with large fractional bandwidths.

Figure 4.34 shows the attenuation slope using the f_0 and σ estimates. Therefore, the total error in the attenuation slope estimate will be the sum of the relative errors ($\Delta f_0 + 2\Delta\sigma$). Since the absolute bandwidth of the pulse will not change for attenuation that depends linearly on frequency, the absolute bandwidth could be obtained by fitting a Gaussian function to

the power spectrum from a reflection of a strong reflector. The error of the attenuation slope estimates would then be only defined by the error in the df/dz estimates. Figure 4.38 shows the error of the attenuation slope assuming σ could be measured without error.

Figure 4.39 shows the error curves ($|error f_0| < 10\%$), which have a variance of less than 13%, 20%, and 30%, as a function of analysis depth (cm) and absolute bandwidth. It can clearly be seen that higher precision is obtained for larger analysis depths. In order to overcome constraints of small analysis depths, high bandwidth pulses need to be used.

4.5 Estimation Error for Different Attenuation Slopes

The amount of downshift of a pulse propagating through an attenuating medium is proportional to the attenuation slope (see equation 2.25). Three different virtual phantoms with attenuation slopes of 0.5, 1.0, and 1.5 dB/cm-MHz were created and interrogated with Gaussian pulses with fractional bandwidth from 20% to 65%, and ranges of center frequencies of 12 - 22, 8 - 14, and 4 - 8 MHz were used for the 0.5, 1.0, and 1.5 dB/cm-MHz phantoms, respectively. The maximum error in the rate of downshift of the pulse center frequency per unit length (df/dz) as a function of the center frequency of the emitted pulse and the analysis depth (dz) is shown in Figure 4.40 for different attenuation slopes. The maximum error was chosen because for each pulse center frequency several fractional bandwidths exist. The maximum standard deviation of df/dz is shown in Figure 4.41.

From Figure 4.40 it can be seen that the error of the df/dz estimates decreases with larger analysis depth (dz). It is also apparent that for larger attenuation slope values the error of the df/dz estimates decreases (note the different scales of the color bar in Figure 4.40). This may lead to the conclusion that a larger attenuation leads to a greater downshift of the pulse. However, the center frequencies of the pulses for each individual virtual phantom were chosen so that the amount of the pulse's downshift was approximately the same for all virtual phantoms. Another explanation may be that the simulated pulses were created so that the maximum amplitude in the time domain was unity. Since different ranges of center

frequencies were used for each virtual phantom, the initial amplitude of the Gaussian pulses will be different. For the 0.5 dB/cm-MHz phantom, pulses with the highest frequency range (12 to 22 MHz) were used and therefore the initial spectral amplitude will be the lowest since the energies in the time and frequency domains have to be equal. It is hypothesized that higher spectral amplitudes of the peak give more accurate estimation results.

4.6 Attenuation Slope Estimates from Physical Phantoms

Two physical phantoms (phantom A and B) were scanned with two single element transducers with nominal center frequencies of 3.5 and 7.5 MHz. Each scan contained 400 RF lines, and five regions of interest were created to obtain five attenuation slope estimates. The region of interest had a lateral overlap of 90% and the number of RF lines used for each individual estimate was varied from 4 to 390. The average attenuation slopes and standard deviations from the five individual estimates as a function of the number of RF lines are shown in Figures 4.42 and 4.43 for phantoms A and B respectively.

From Figures 4.42 and 4.43 it can be seen that no accurate attenuation slope estimates could be obtained for the 3.5 MHz transducer. One of the main differences between the two transducers is the absolute bandwidth. In order to estimate the absolute bandwidth of the transducers a Gaussian function was fitted to the reference signal obtained at the focus (see Figure 4.44). The estimated absolute bandwidths were 1.02 and 1.79 MHz for the 3.5 and 7.5 MHz transducers respectively. Calculating the amount of downshift for these two transducers gives 0.191 and 0.727 MHz for a medium with an attenuation slope of 0.4 dB/cm-MHz. Looking at the maximum error of df/dz as a function of the downshift (df) at the analysis depth for the simulated data shows that estimation errors up to 100% can occur for a downshift of about 0.2 MHz (see Figure 4.45). Another explanation for the weak performance of the 3.5 MHz transducer may be that the shape of the pulse seems to deviate more from the Gaussian assumption than the 7.5 MHz pulse (see Figure 4.44). Also, the $f/\#$ ($f/\# =$ focal distance/aperture diameter) for both transducers is different (3.5

MHz, $f/\# = 3$ and 7.5 MHz, $f/\# = 4$), which could mean that the diffraction correction works better for higher $f/\#$ s.

4.7 Figures

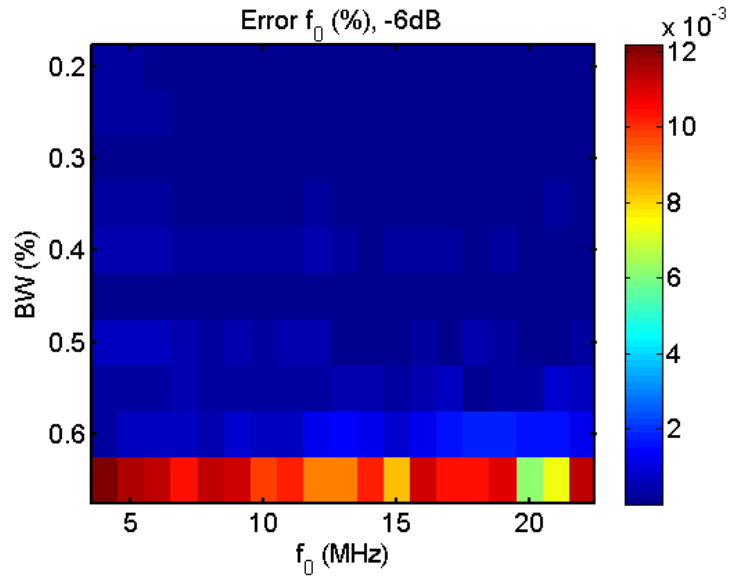


Figure 4.1: Absolute error (%) of the estimated center frequency (f_0).

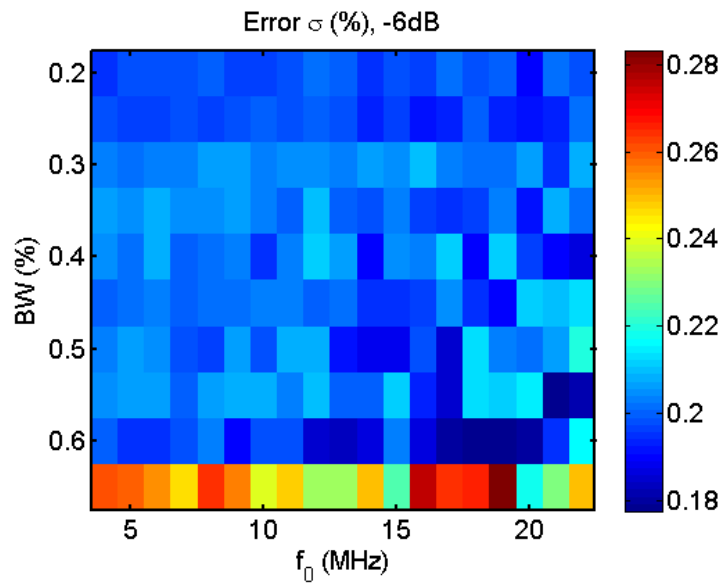


Figure 4.2: Absolute error (%) of the estimated absolute bandwidth (σ).

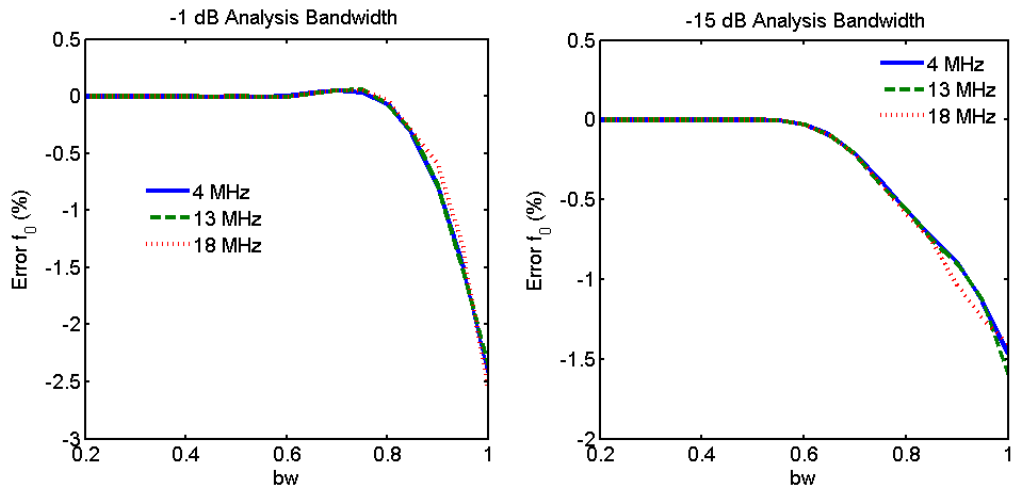


Figure 4.3: Error of f_0 as a function of fractional bandwidth for a -1 and -15 dB analysis bandwidth.

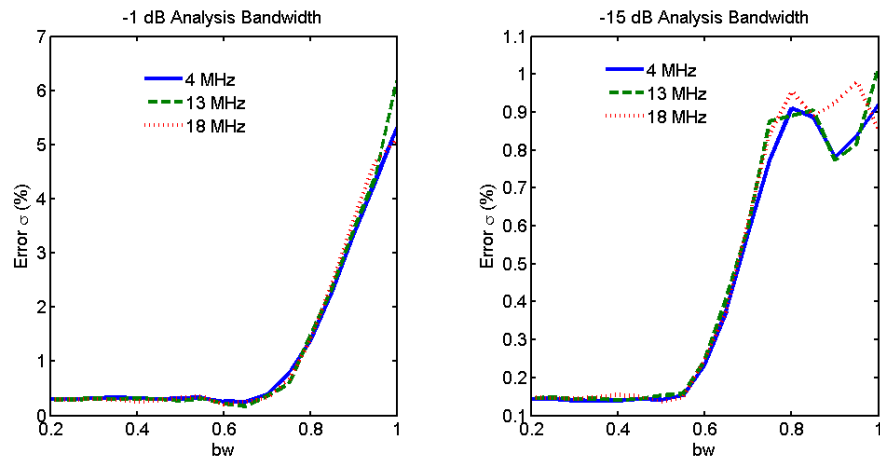


Figure 4.4: Error of σ as a function of fractional bandwidth for a -1 and -15 dB analysis bandwidth.

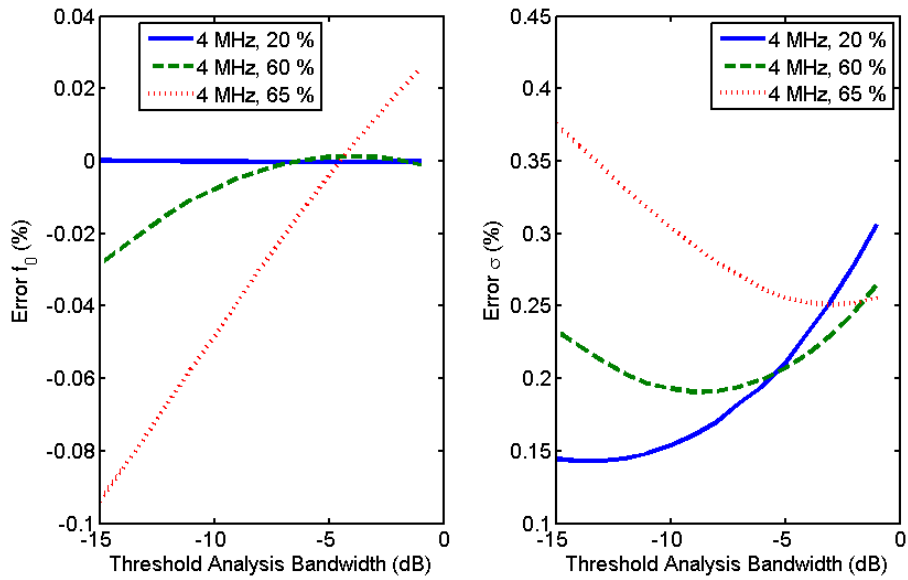


Figure 4.5: Error of f_0 and σ as a function of analysis bandwidth.

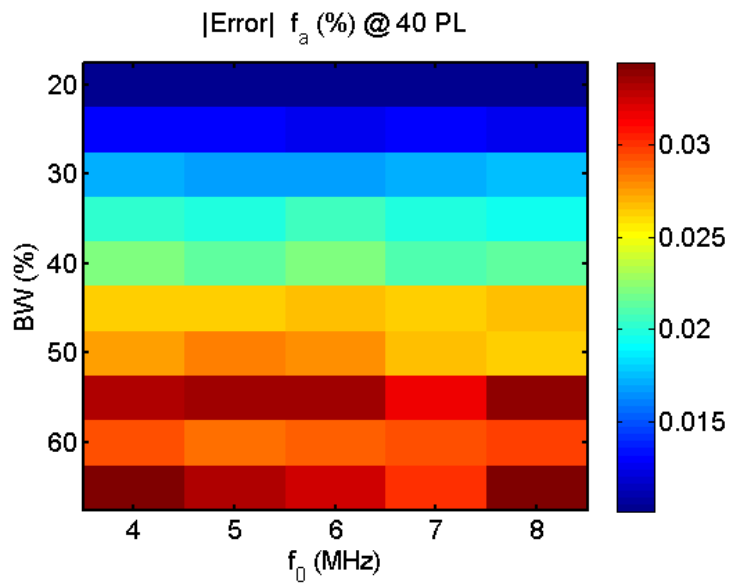


Figure 4.6: Absolute error of the estimated center frequency (f_0) of a Gaussian pulse propagating in an attenuating medium with an attenuation slope of 1.5 dB/cm-MHz. The estimates were obtained at a depth of 40 PL .

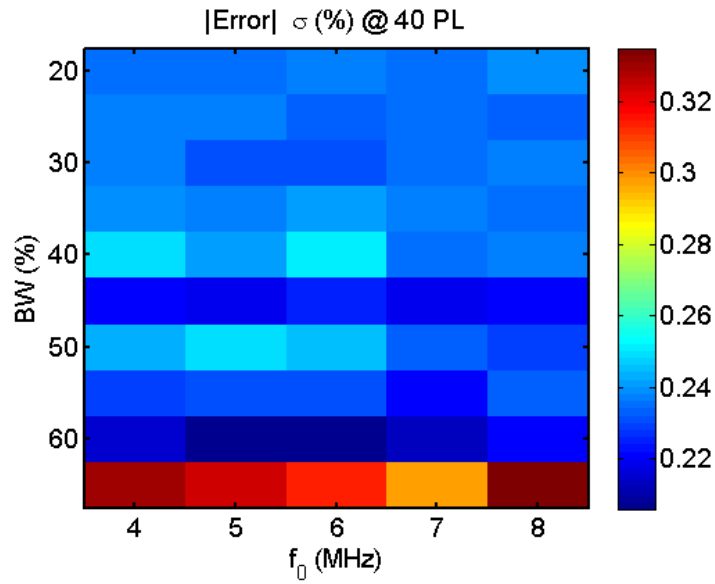


Figure 4.7: Absolute error of the estimated absolute bandwidth (σ) of a Gaussian pulse propagating in an attenuating medium with an attenuation slope of 1.5 dB/cm-MHz. The estimates were obtained at a depth of 40 PL .

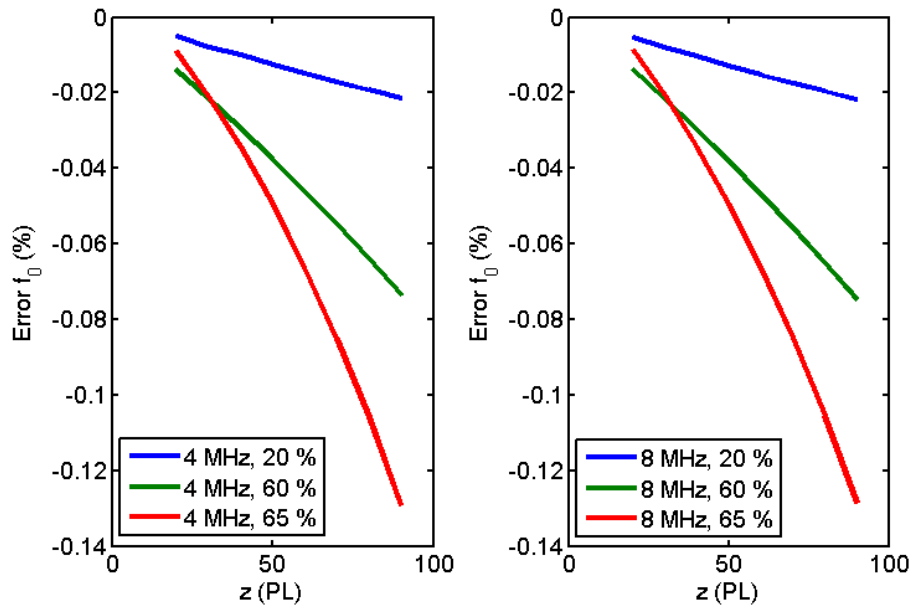


Figure 4.8: Error of f_0 as a function of depth in terms of PL . The attenuation slope of the medium was 1.5 dB/cm-MHz.

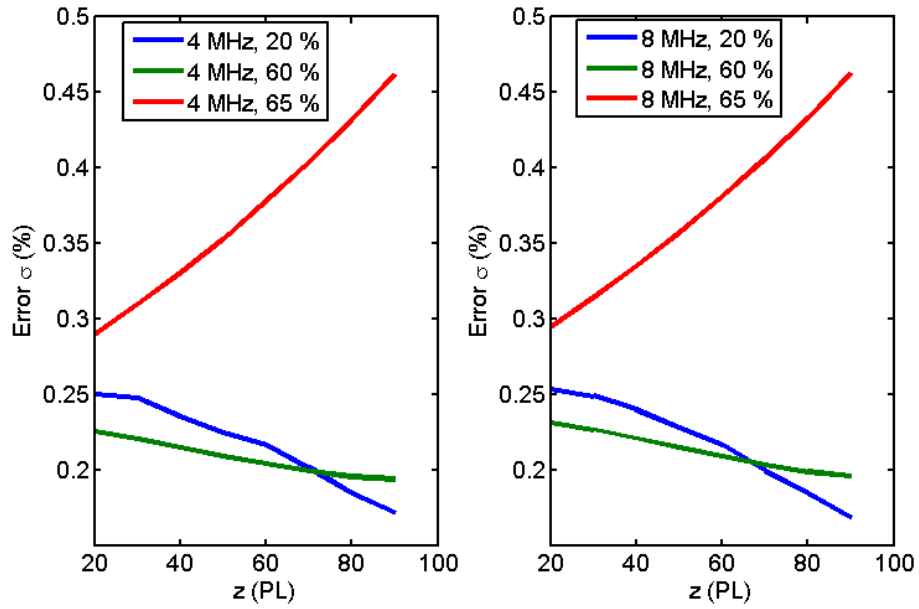


Figure 4.9: Error of σ as a function of depth in terms of PL . The attenuation slope of the medium was 1.5 dB/cm-MHz.

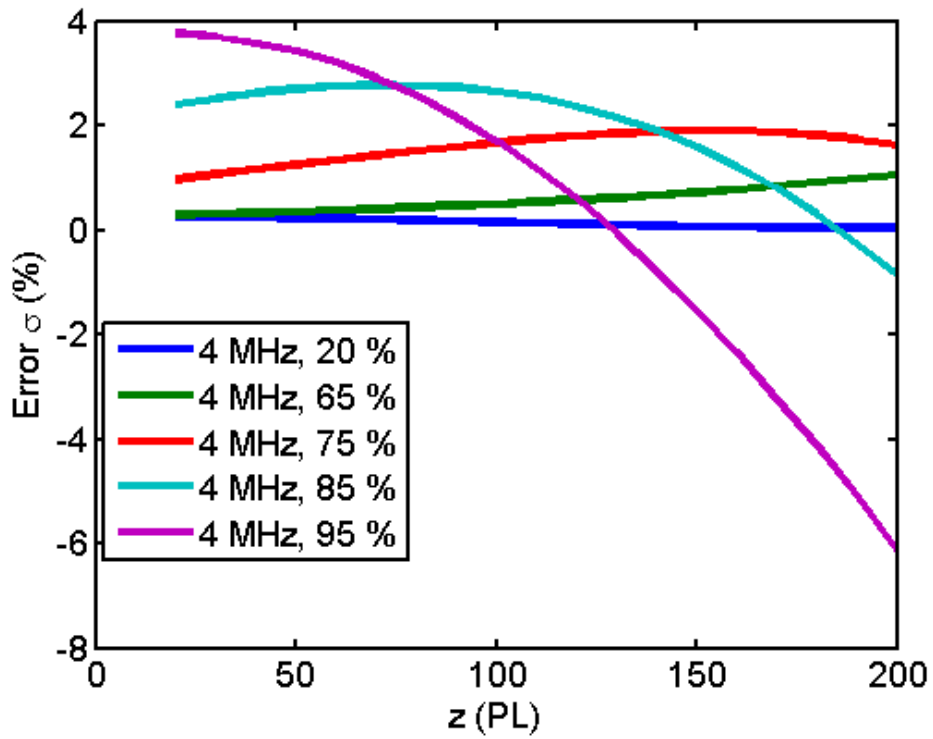


Figure 4.10: Error of σ as a function of depth in terms of PL . The attenuation slope of the medium was 1.5 dB/cm-MHz.

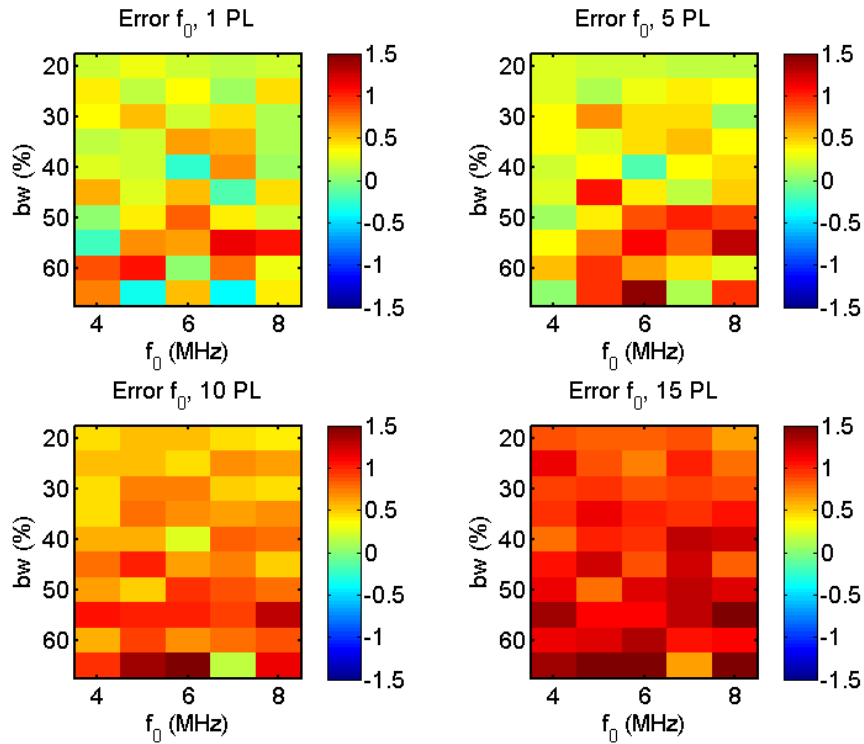


Figure 4.11: Error of the f_0 estimates obtained from an attenuating medium for different window lengths in terms of pulse lengths (top left 1 PL , top right 5 PL , bottom right 10 PL , and bottom right 15 PL). The attenuation slope of the medium was 1.5 dB/cm-MHz. The analysis bandwidth was defined by the -1.5 dB drop relative to the peak of the pulse.

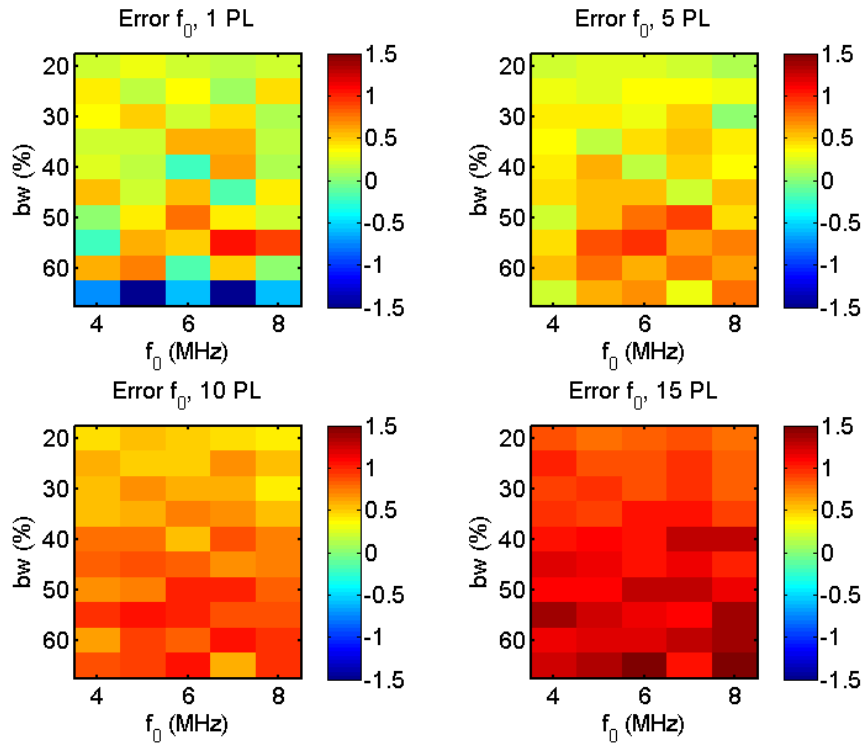


Figure 4.12: Error of the f_0 estimates obtained from an attenuating medium for different window lengths in terms of pulse lengths (top left 1 PL , top right 5 PL , bottom left 10 PL , and bottom right 15 PL). The attenuation slope of the medium was 1.5 dB/cm-MHz. The analysis bandwidth was defined by the -3 dB drop relative to the peak of the pulse.

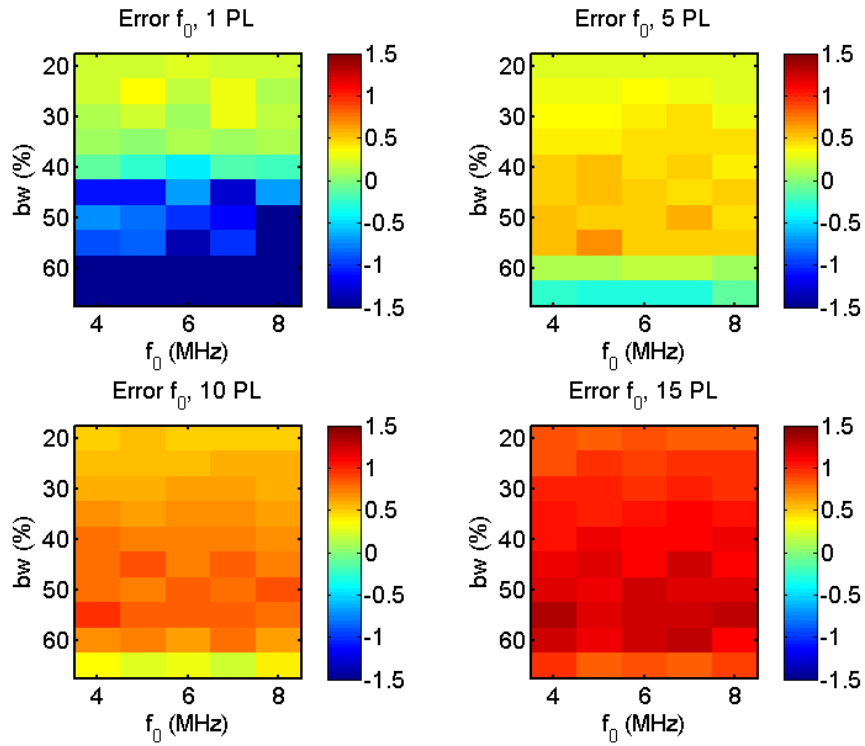


Figure 4.13: Error of the f_0 estimates obtained from an attenuating medium for different window lengths in terms of pulse lengths (top left 1 PL , top right 5 PL , bottom left 10 PL , and bottom right 15 PL). The attenuation slope of the medium was 1.5 dB/cm-MHz. The analysis bandwidth was defined by the -12 dB drop relative to the peak of the pulse.

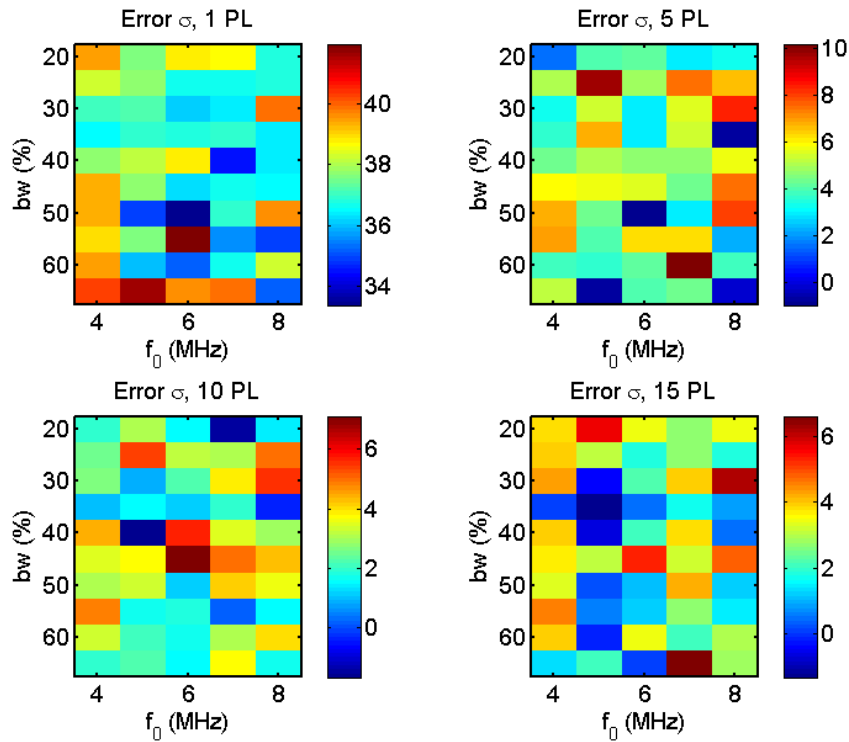


Figure 4.14: Error of the σ estimates obtained from an attenuating medium for different window lengths in terms of pulse lengths (top left 1 PL , top right 5 PL , bottom left 10 PL , and bottom right 15 PL). The attenuation slope of the medium was 1.5 dB/cm-MHz. The analysis bandwidth was defined by the -1.5 dB drop relative to the peak of the pulse.

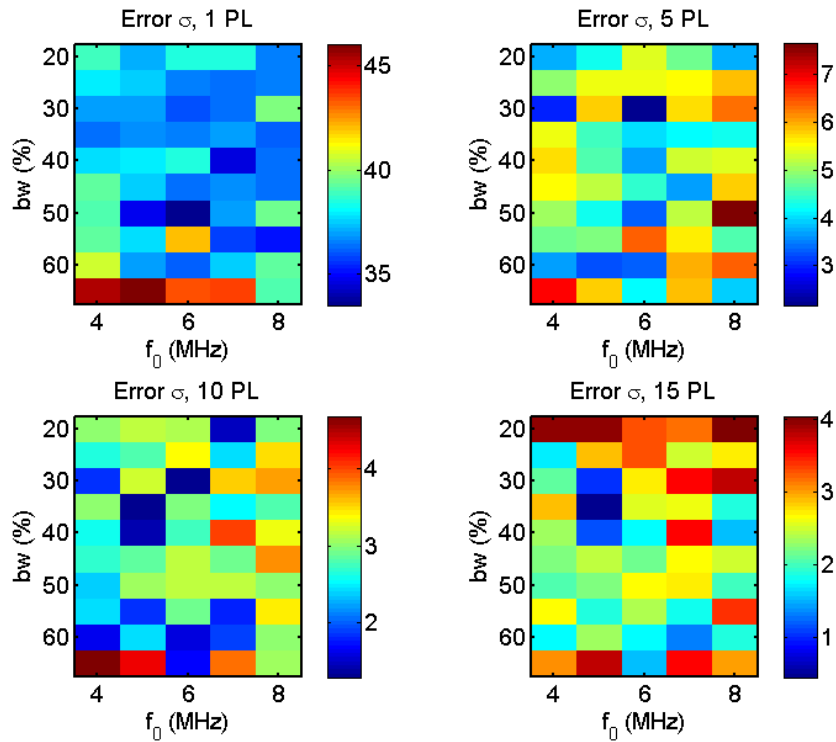


Figure 4.15: Error of the σ estimates obtained from an attenuating medium for different window lengths in terms of pulse lengths (top left 1 *PL*, top right 5 *PL*, bottom left 10 *PL*, and bottom right 15 *PL*). The attenuation slope of the medium was 1.5 dB/cm-MHz. The analysis bandwidth was defined by the -3 dB drop relative to the peak of the pulse.

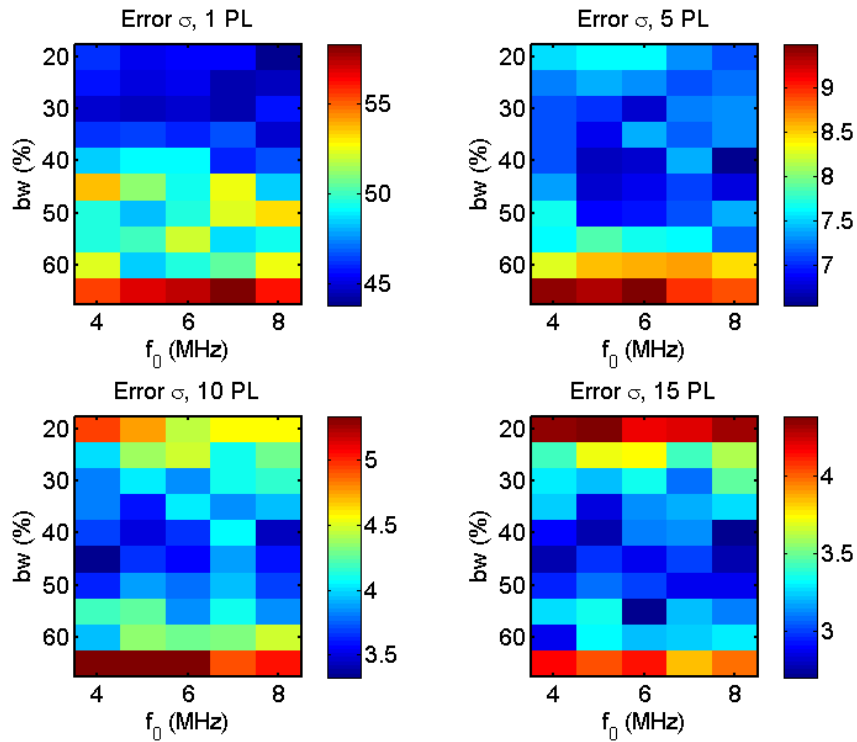


Figure 4.16: Error of the σ estimates obtained from an attenuating medium for different window lengths in terms of pulse lengths (top left 1 *PL*, top right 5 *PL*, bottom left 10 *PL*, and bottom right 15 *PL*). The attenuation slope of the medium was 1.5 dB/cm-MHz. The analysis bandwidth was defined by the -12 dB drop relative to the peak of the pulse.

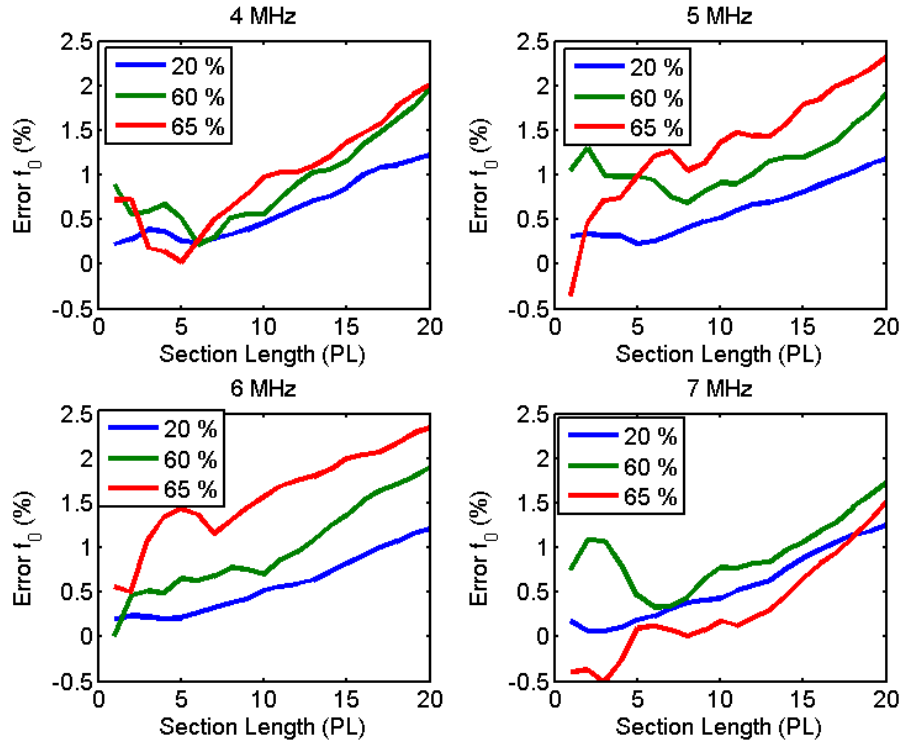


Figure 4.17: Error of f_0 estimates as a function of the gate length (section length) in terms of PL. The analysis bandwidth corresponded to the -1.5 dB fall off.

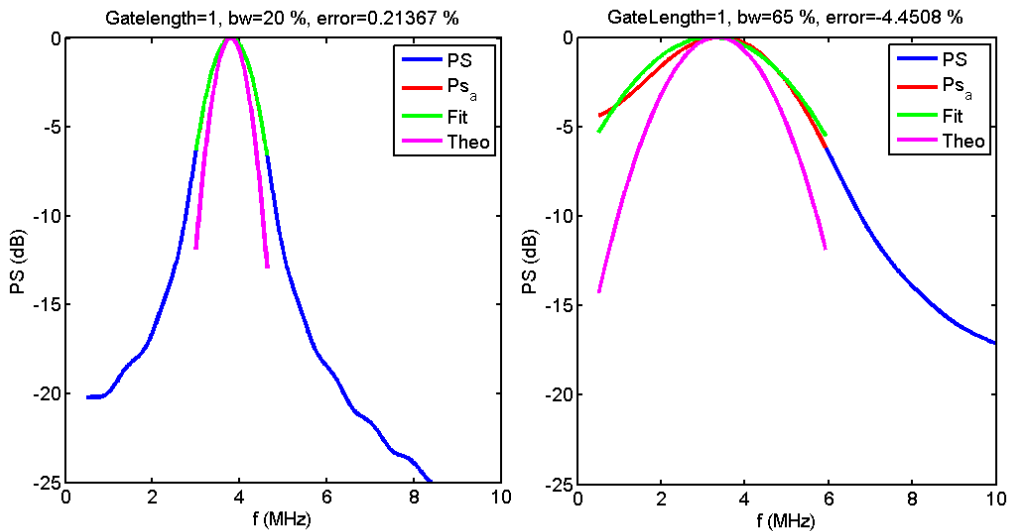


Figure 4.18: Effect of spectral broadening due to a short gate length (section length) (1 PL) shown for a 4 MHz pulse with a fractional bandwidth of 20% (left) and 65% (right).

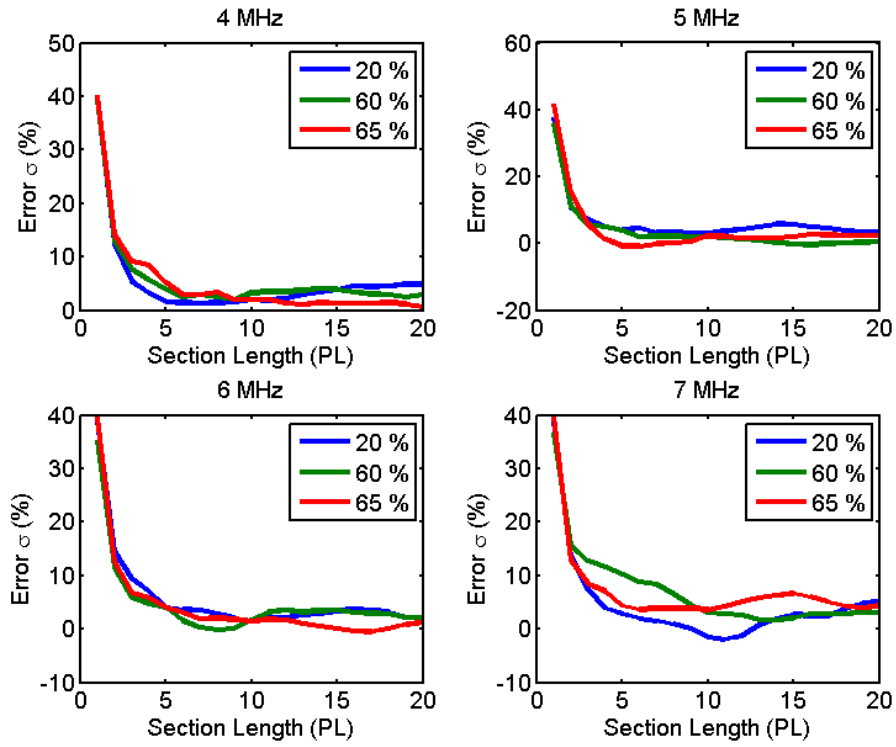


Figure 4.19: Error of σ estimates as a function of the gate length (section length) in terms of PL. The analysis bandwidth corresponded to the -1.5 dB fall off.

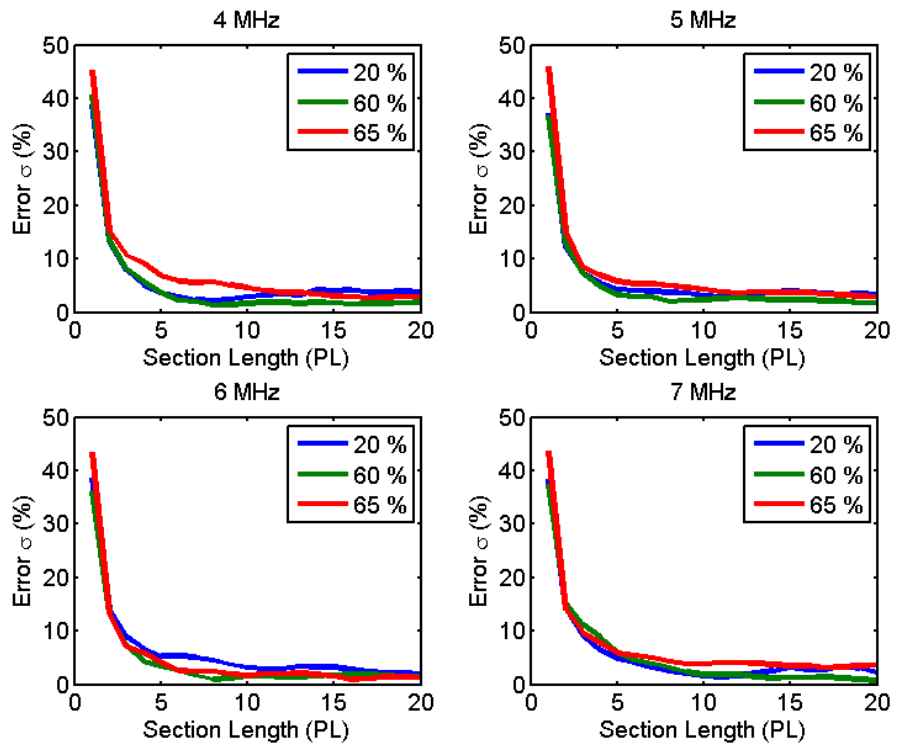


Figure 4.20: Error of σ estimates as a function of the gate length (section length) in terms of PL. The analysis bandwidth corresponded to the -3 dB fall off.

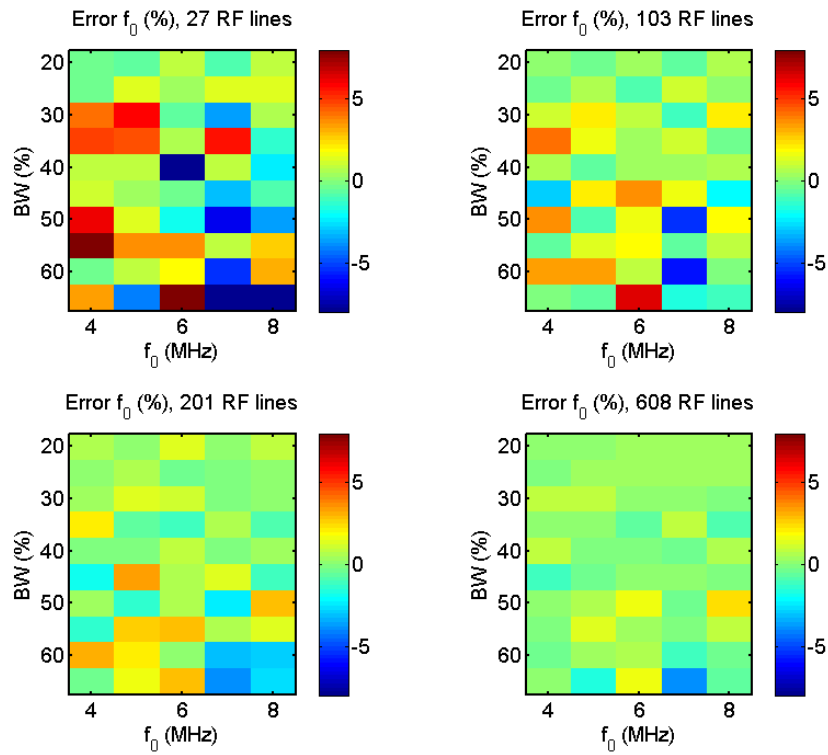


Figure 4.21: Error of f_0 estimates for a gate length of one pulse length and an analysis bandwidth corresponding to -3 dB.

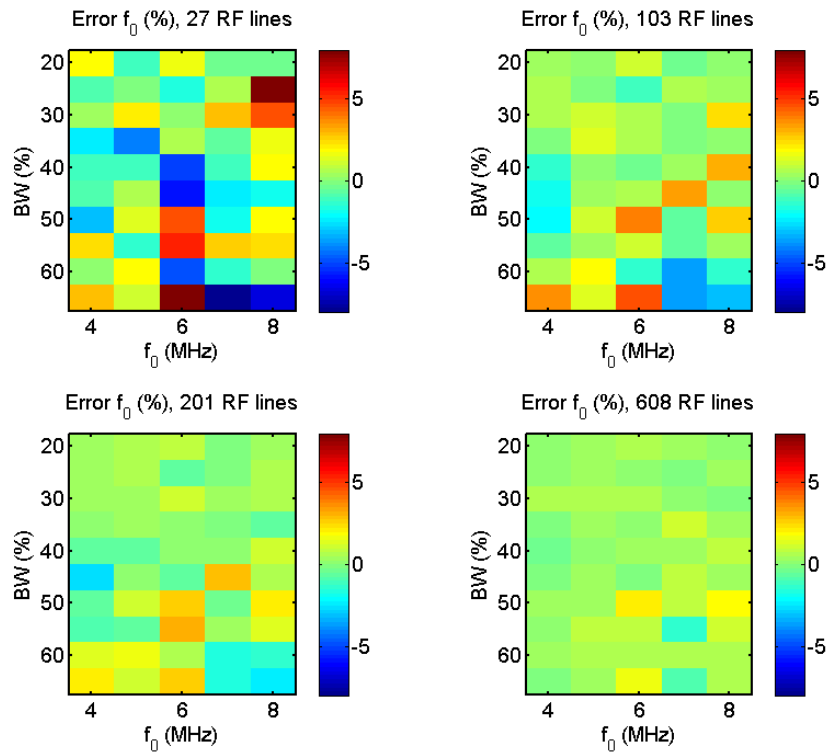


Figure 4.22: Error of f_0 estimates for a gate length of five pulse lengths and an analysis bandwidth corresponding to -3 dB.

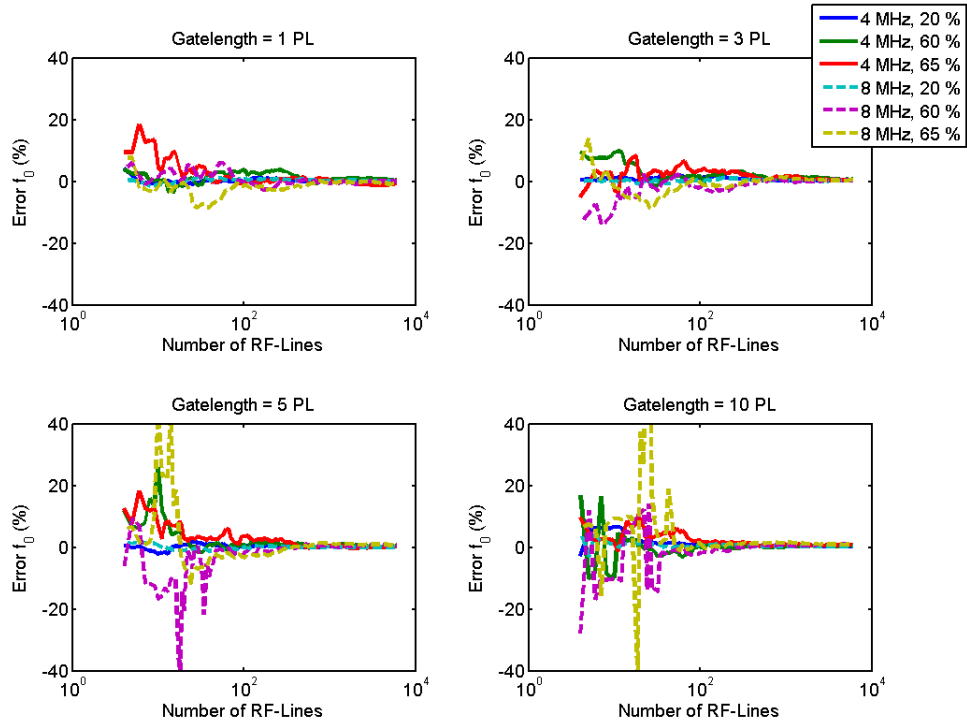


Figure 4.23: Estimated error in f_0 as a function of number of averaged RF lines.

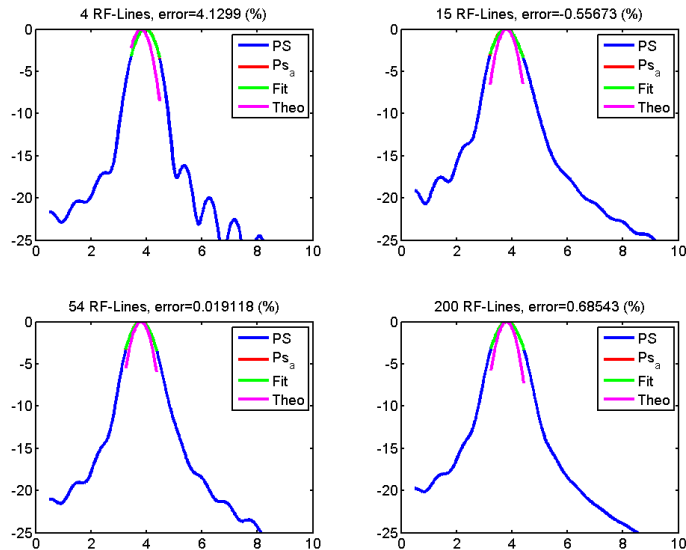


Figure 4.24: Power spectra of a 4 MHz pulse with a fractional bandwidth of 20%. The gate length was 1 PL .

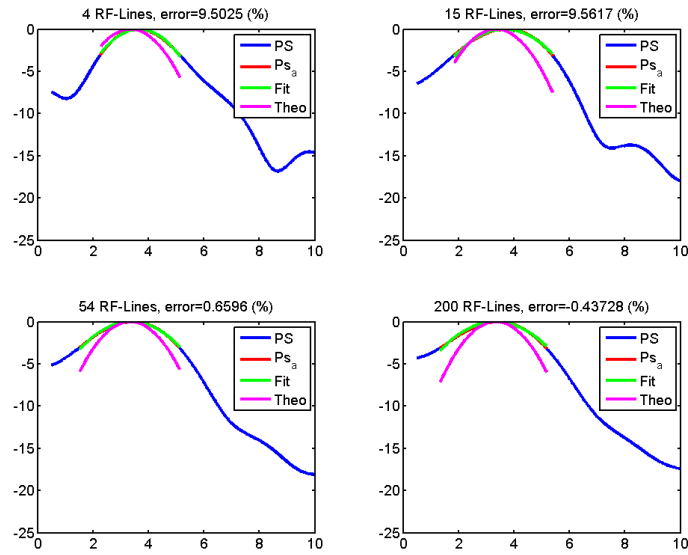


Figure 4.25: Power spectra of a 4 MHz pulse with a fractional bandwidth of 65%. The gate length was 1 PL .

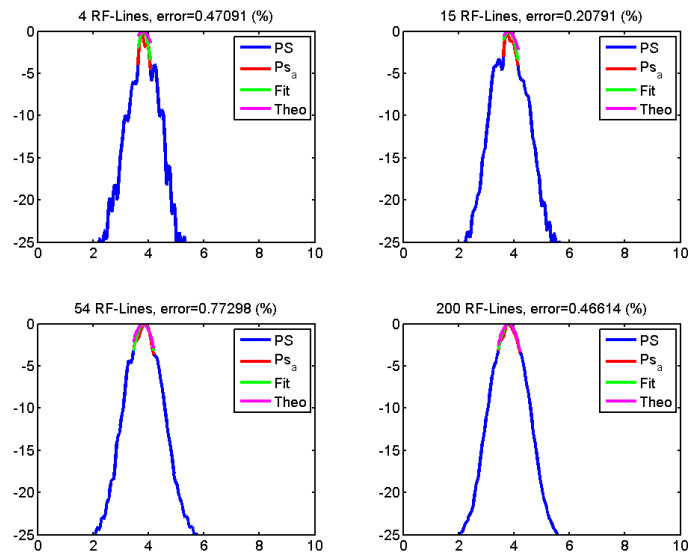


Figure 4.26: Power spectra of a 4 MHz pulse with a fractional bandwidth of 20%. The gate length was 5 PL .

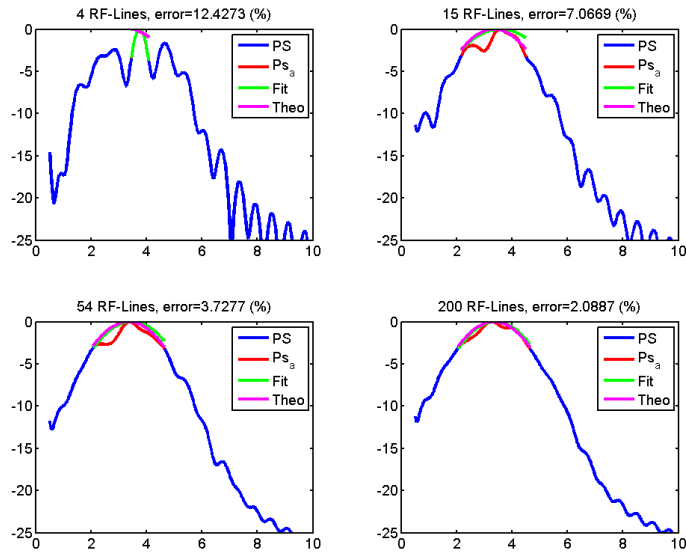


Figure 4.27: Power spectra of a 4 MHz pulse with a fractional bandwidth of 65%. The gate length was $5 PL$.

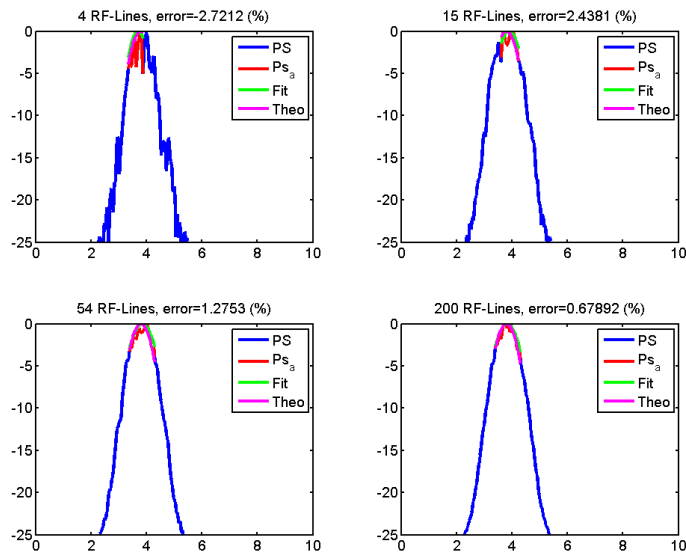


Figure 4.28: Power spectra of a 4 MHz pulse with a fractional bandwidth of 20%. The gate length was $10 PL$.

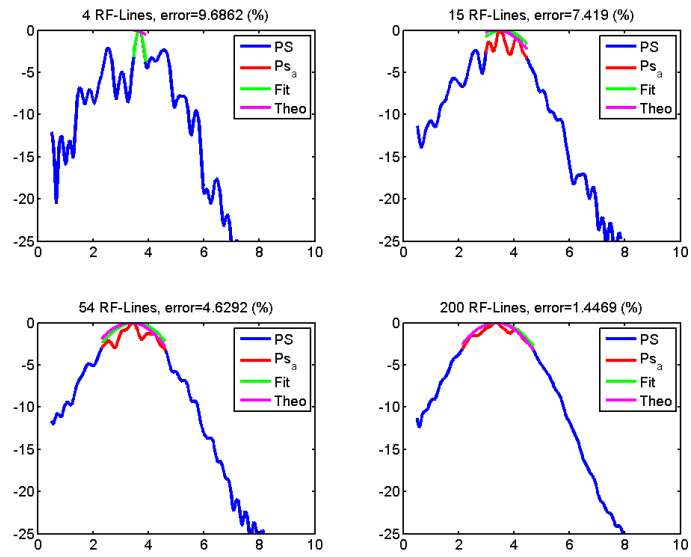


Figure 4.29: Power spectra of a 4 MHz pulse with a fractional bandwidth of 65%. The gate length was 10 PL .

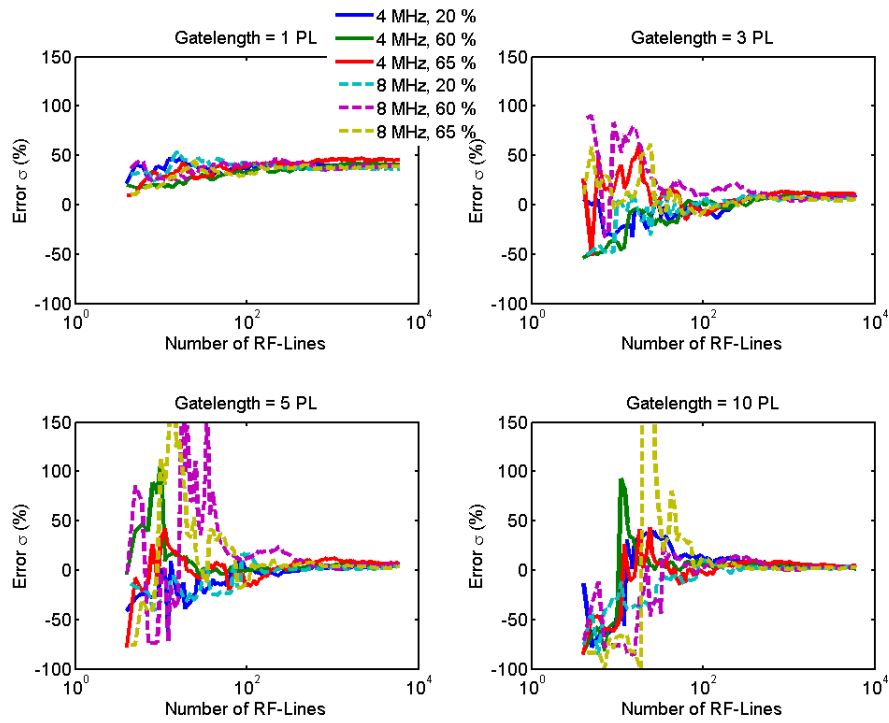


Figure 4.30: Estimated error of σ as a function of number of averaged RF lines.

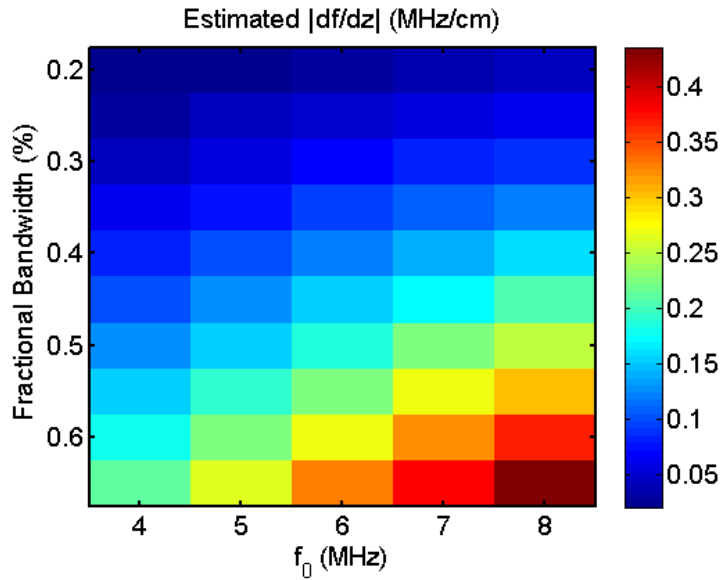


Figure 4.31: Estimated df_α/dz for region of interest of 600 RF lines and a depth of 50 PL.

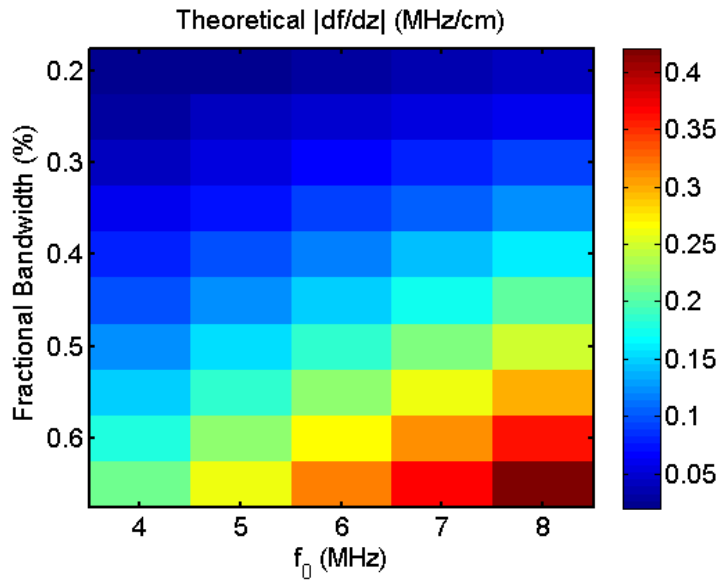


Figure 4.32: Estimated df_α/dz for region of interest of 600 RF lines and a depth of 50 PL .

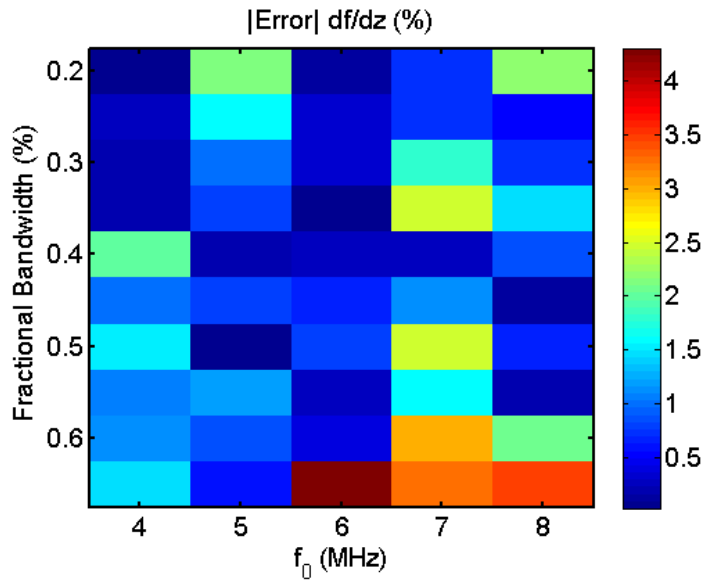


Figure 4.33: Absolute error (%) of the f_0 estimates.

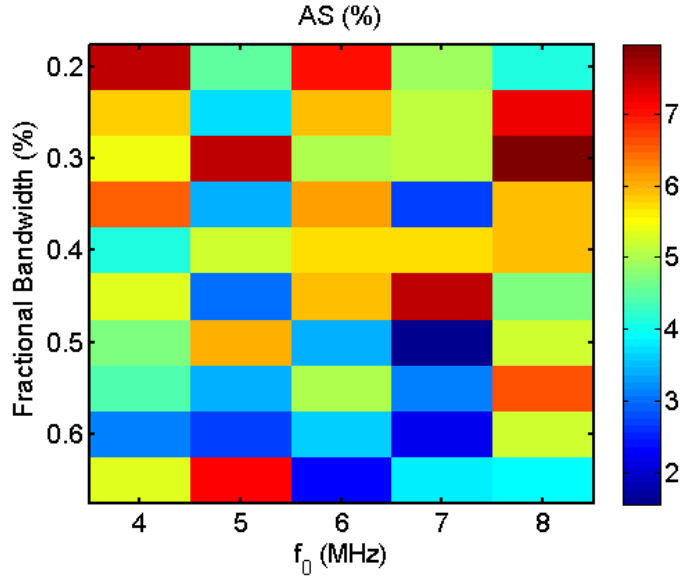


Figure 4.34: Error of the attenuation slope estimates computed from the df/dz and σ estimates.

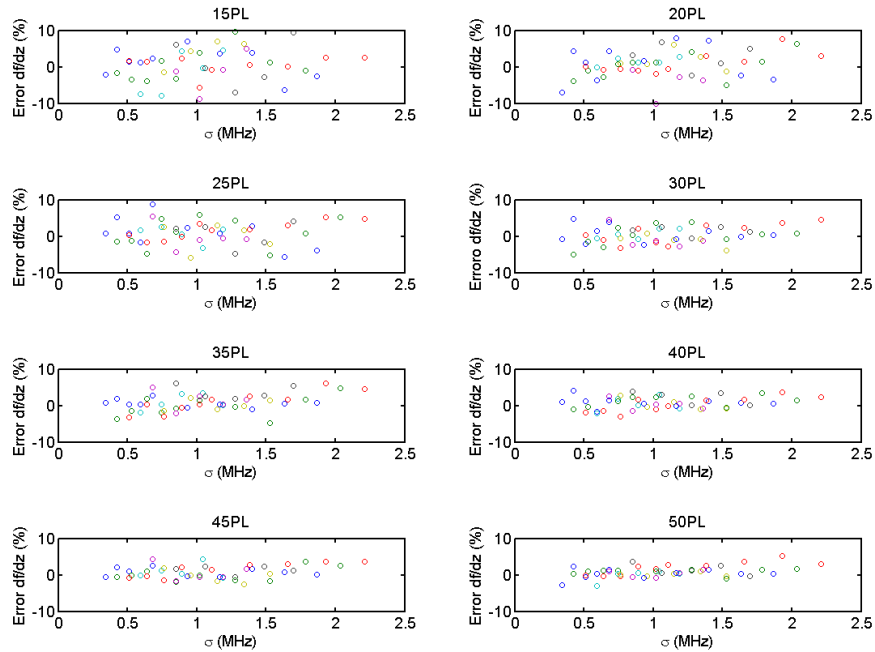


Figure 4.35: Error in the df/dz estimates as a function of the absolute bandwidth σ . The axial analysis region was increased from 15 to 50 PL . The displayed error is an average obtained from 100 samples. The lateral size of the region of interest was 60 RF lines.

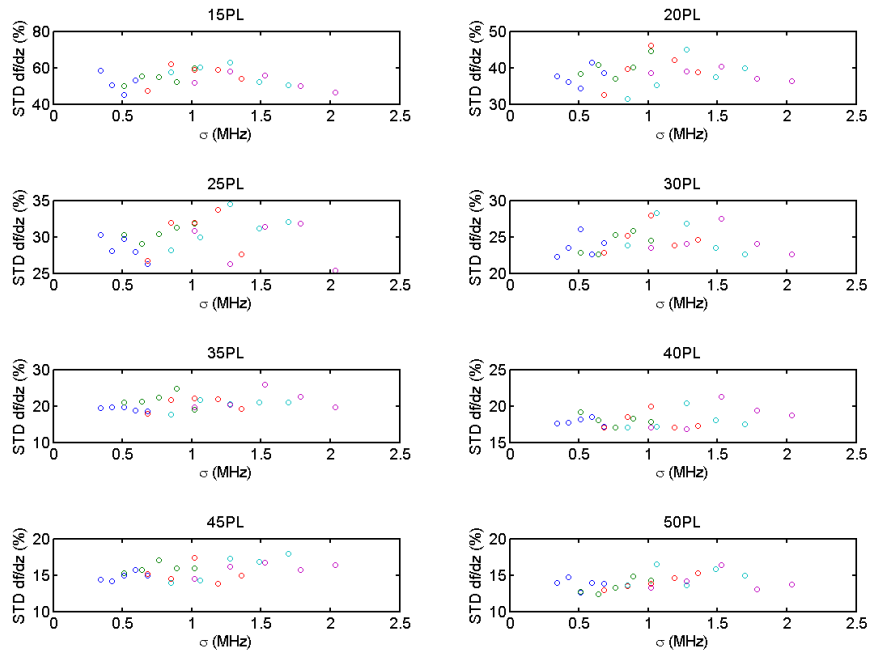


Figure 4.36: Standard deviation of the df/dz estimates as a function of the absolute bandwidth σ . The axial analysis region was increased from 15 to 50 PL . The displayed error is an average obtained from 100 samples. The lateral size of each individual region of interest was 60 RF lines.

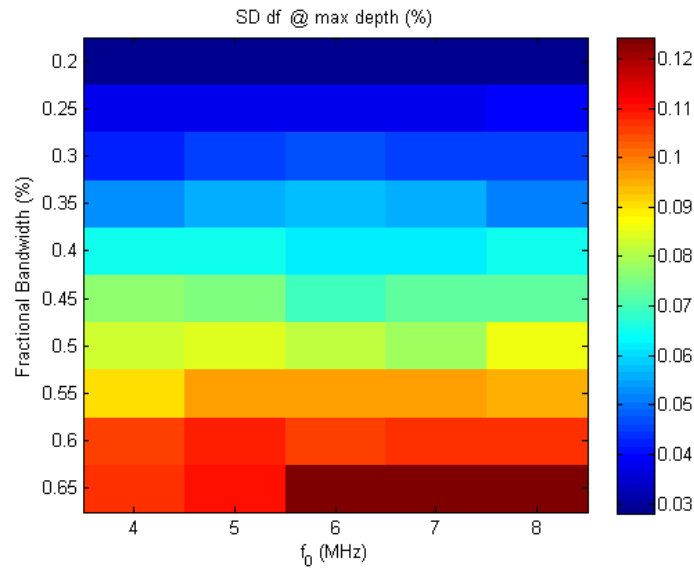


Figure 4.37: Standard deviation of the downshift (df) estimates obtained from the gate at a depth of 50 PL . The standard deviation was obtained from 100 samples.

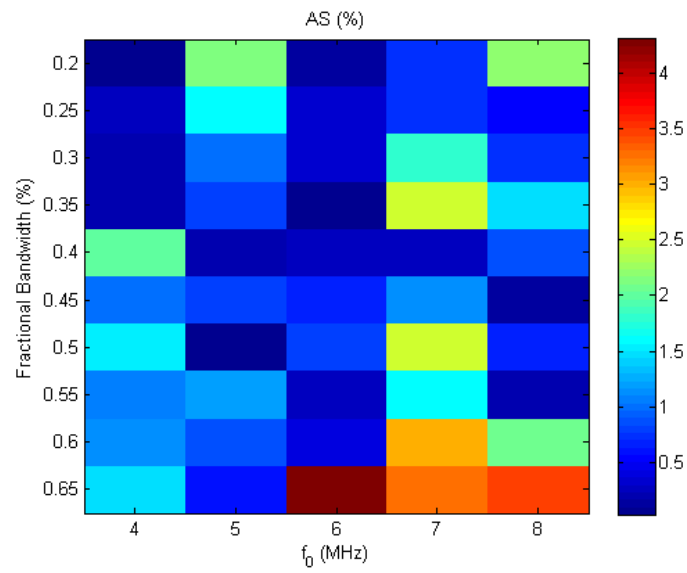


Figure 4.38: Absolute error of the attenuation slope estimate assuming σ can be obtained with a negligible error from a reference.

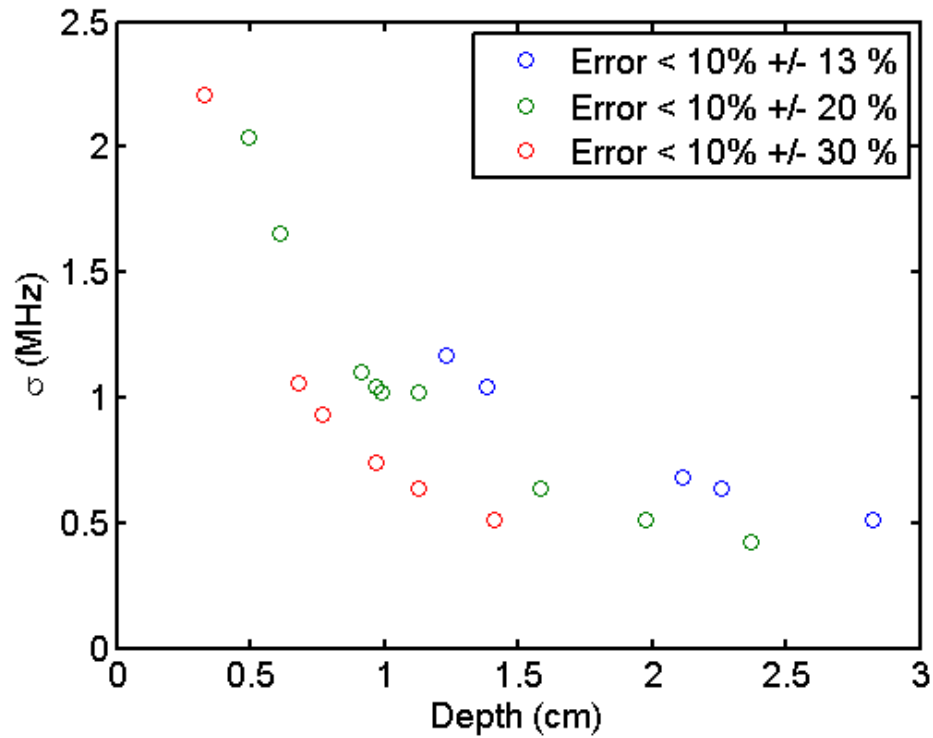


Figure 4.39: Error curves for different precisions. The blue dots represent attenuation slope estimates which had an error less than 10% and standard deviation less than 13%. The green dots represent attenuation slope estimates which had an error less than 10% and standard deviation less than 20%. The red dots represent attenuation slope estimates which had an error less than 10% and standard deviation less than 30%.

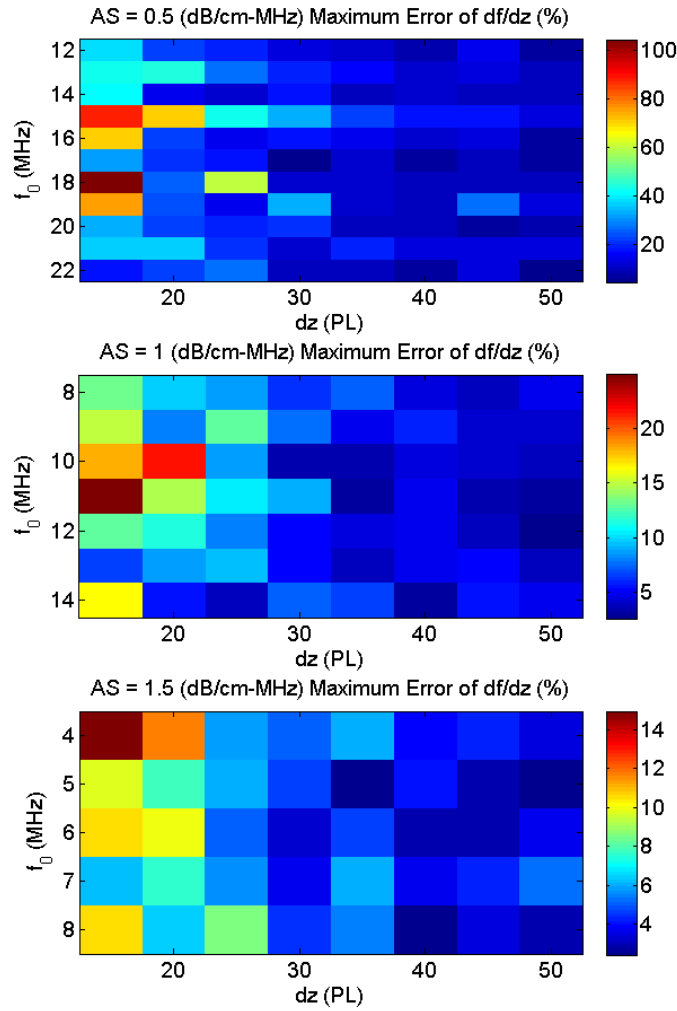


Figure 4.40: Maximum error in the rate of downshift of the pulse center frequency per unit length (df/dz) as a function of analysis depth and center frequency of the pulse. The relative error is shown for a medium with an attenuation slope of 0.5 (top), 1.0 (middle), and 1.5 dB/cm-MHz (bottom).

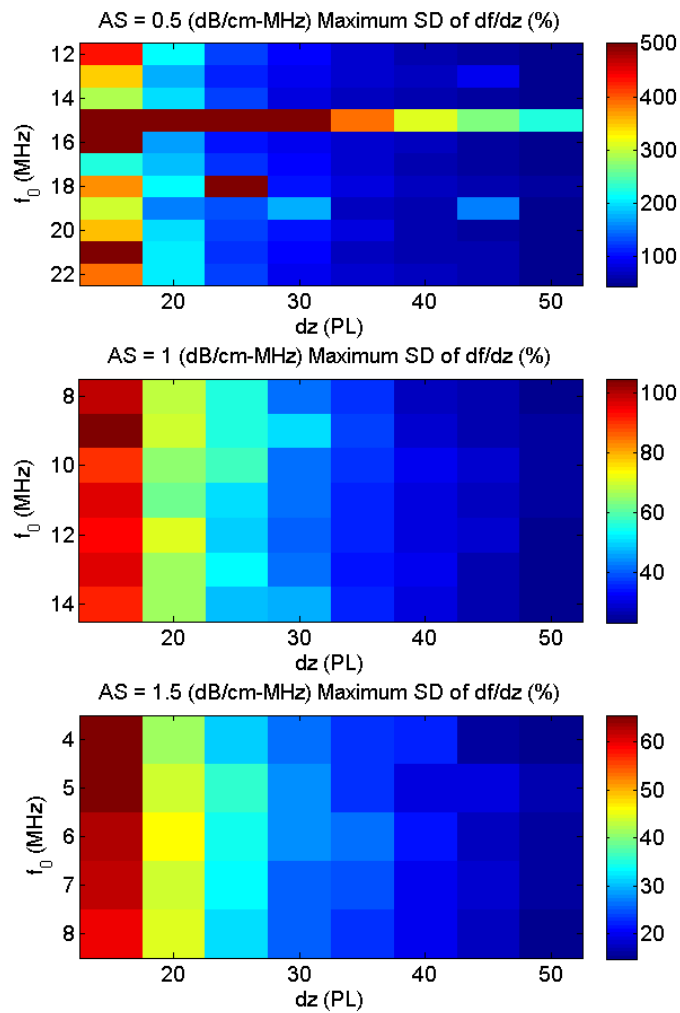


Figure 4.41: Maximum standard deviation of the rate of downshift of the pulse center frequency per unit length (df/dz) as a function of analysis depth and center frequency of the pulse. The relative error is shown for a medium with a attenuation slope of 0.5 (top), 1.0 (middle), and 1.5 dB/cm-MHz (bottom).

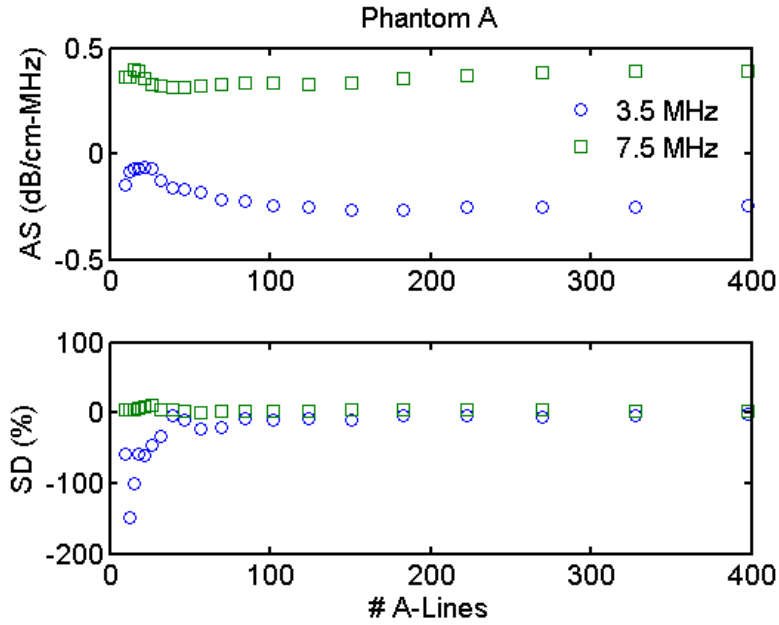


Figure 4.42: Average attenuation slope and standard deviation for phantom A (0.42 dB/cm-MHz) for two single-element transducer (3.5 and 7.5 MHz).

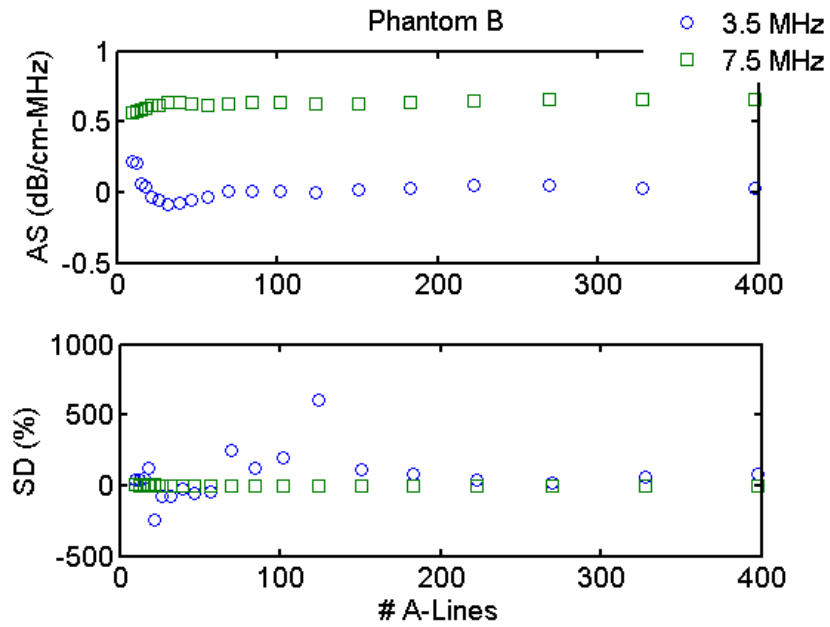


Figure 4.43: Average attenuation slope and standard deviation for phantom B (0.67 dB/cm-MHz) for two single-element transducer (3.5 and 7.5 MHz).

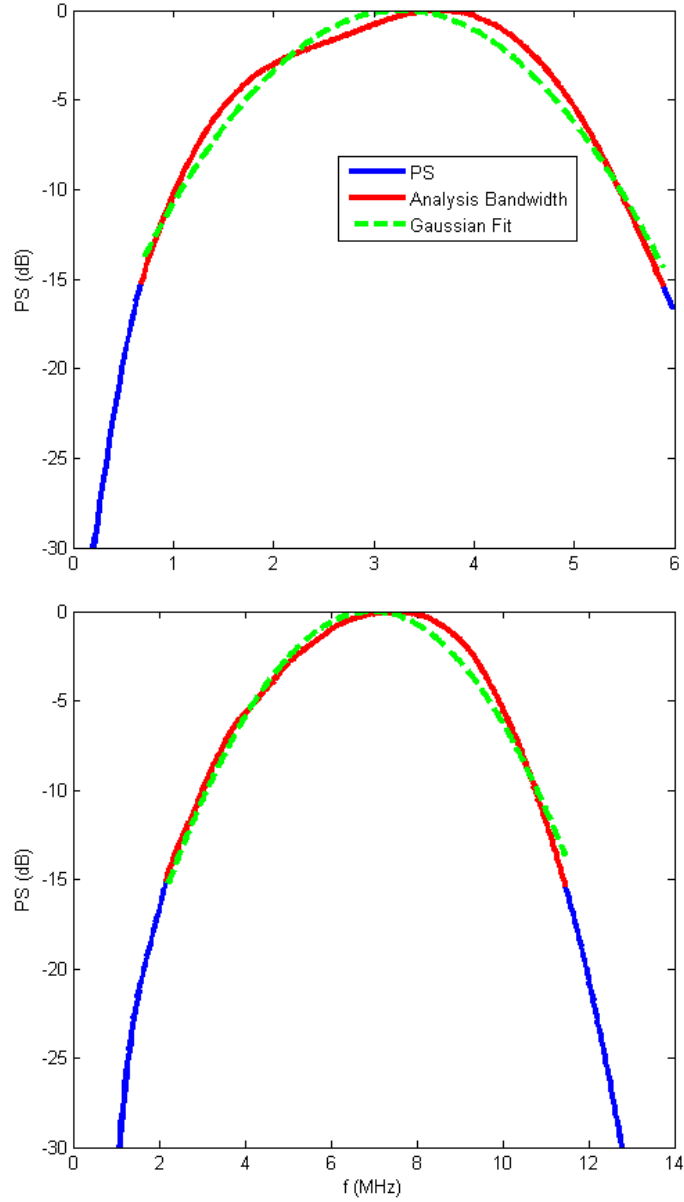


Figure 4.44: Power spectrum obtained from a reflection upon a planar surface at the transducer focus for the 3.5 (top) and 7.5 MHz (bottom) transducers.

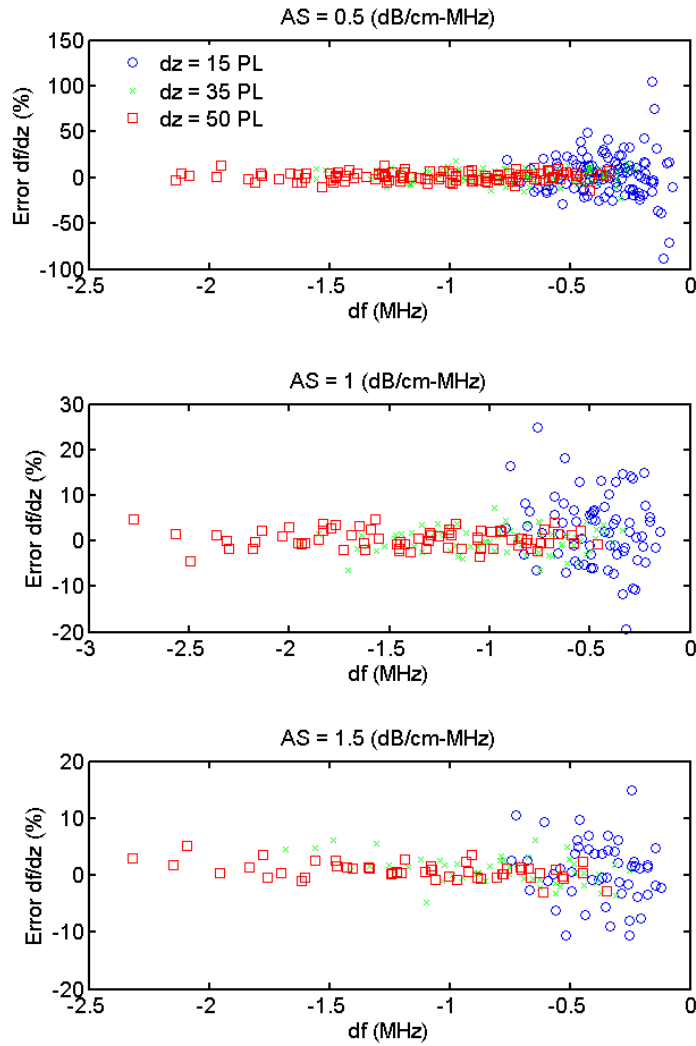


Figure 4.45: Maximum error of the df/dz estimate as a function of df for virtual phantoms with 0.5 (top), 1.0 (middle), and 1.5 dB/cm-MHz (bottom) attenuation slope.

CHAPTER 5

CONCLUSION

Utilizing the downshift of the pulse center frequency to estimate the attenuation slope is a unique tool to study tissue ultrasonically. This work concentrated on the accuracy and precision of the attenuation estimates and investigated limiting parameters such as analysis depth, absolute bandwidth and attenuation slope of the medium utilizing simulations.

The RF data from virtual phantoms was created using a phase consisting of a linear and a minimum phase term. The fact that media with a linear frequency dependency have a minimum phase was shown by Kuc et al. on the example of Plexiglas [17]. However, it is arguable whether this one experiment is enough evidence to validate this assumption. Kuc et al. also state that the filter may introduce distortions to the power spectra for high attenuation values [17]. In this work we could not find any evidence of distorted spectra. Since the phase information is disregarded in the algorithm and the computational expense is high for the Hilbert transformation, the minimum phase filter approach may be neglected and only a linear phase filter may be used.

It has been shown that fitting a Gaussian function to the power spectra in order to obtain the center frequency and width of the pulse is not necessarily the optimal approach. The estimation performance decreases significantly for pulses with a high fractional bandwidth and introduces an additional error. The estimation accuracy seems also be altered by the spectral amplitude of the pulse. Therefore, it could not be shown that increasing the bandwidth leads to more accurate or precise estimates. Other approaches such as the spectral centroid [15] or cross correlation techniques [6] may provide better results.

However, it could be shown that increasing the depth of analysis increases the amount of downshift of the center frequency of the pulse and therefore the accuracy and precision of the estimates. In order to achieve a

certain accuracy and precision, the absolute bandwidth has to be chosen according to the analysis depth, as illustrated by Figure 4.39.

It was experimentally shown that the attenuation slope can be accurately estimated when a transducer with a sufficient absolute bandwidth is used. However, deviation of the spectral amplitude from a Gaussian shape and the influence of the diffraction correction of the estimation results need to be further investigated. Filtering the spectral ratio with a Gaussian filter, with parameters close to the transducer properties instead of the transducer impulse response obtained at the focus, may give better results.

The spectral shift method discussed here has several assumptions incorporated in it, such as linear frequency dependency of the attenuation and Gaussian shape of the pulse, which limit this approach to a very specific set of applications. A linear frequency dependency of the attenuation can even be assumed for media with no linear frequency dependency as long as the frequency band is kept small. However, this will lead to small frequency shifts of the pulse center frequency and those will be difficult to detect.

Spatial variation noise alters the spectra and estimates. Reducing the gate length to truncate the RF data introduces a filtering effect of the spectra. This may be used to reduce the size of the analysis region and improve the spatial resolution of the attenuation slope estimates.

APPENDIX A

A.1 Derivation of Gaussian Pulse Propagating through Lossy Medium

The spectral power of a Gaussian pulse propagating through a lossy medium with linear frequency dependency can be expressed as (see equation 2.22)

$$\exp \left[\frac{-(f - f_0)^2}{2\sigma^2} - 4\beta f z_0 \right] = \exp \left[- (f^2 - 2ff_0 + f_0^2 + 8\beta f \sigma^2 z_0) \frac{1}{2\sigma^2} \right]. \quad (\text{A.1})$$

The term in the square brackets on the right-hand side of equation A.1 can be rewritten as

$$f^2 - 2ff_0 + f_0^2 + 8\beta f \sigma^2 z_0 = f^2 - 2f(f_0 - 4\beta \sigma^2 z_0) + f_0^2 \quad (\text{A.2})$$

$$= f^2 - 2ff_\alpha + f_0^2 + f_\alpha^2 - f_\alpha^2 \quad (\text{A.3})$$

$$= (f^2 - 2ff_\alpha + f_\alpha^2) + f_0^2 - f_\alpha^2 \quad (\text{A.4})$$

$$= (f - f_\alpha)^2 + f_0^2 - f_\alpha^2. \quad (\text{A.5})$$

Therefore, it follows for A.1 that

$$\exp \left[- ((f - f_\alpha)^2 + f_0^2 - f_\alpha^2) \frac{1}{2\sigma^2} \right] = \exp \left(- \frac{(f - f_\alpha)^2}{2\sigma^2} \right) \exp \left(- \frac{f_0^2 - f_\alpha^2}{2\sigma^2} \right). \quad (\text{A.6})$$

A.2 Fractional Bandwidth

The -3 dB fractional bandwidth corresponds to the frequencies where the Gaussian shaped pulse falls of to $\frac{1}{\sqrt{2}}$. An implemented Matlab function was used to create the Gaussian pulse with the model $\exp\left[\frac{-(f-b)^2}{c^2}\right]$.

$$\frac{1}{\sqrt{2}} = \exp\left[\frac{-(f-b)^2}{c^2}\right] \quad (\text{A.7})$$

$$\frac{1}{2} \ln\left(\frac{1}{2}\right) = \frac{-(f-b)^2}{c^2} \quad (\text{A.8})$$

$$c = \pm \frac{f-b}{\frac{1}{2} \ln\left(\frac{1}{2}\right)}. \quad (\text{A.9})$$

The term $f-b$ equals to half of the absolute bandwidth (Δf_{-3dB}). Using $\Delta f_{-3dB} = f_0 BW$ gives

$$c = \frac{f_0 BW}{2} \frac{1}{\frac{1}{2} \ln\left(\frac{1}{2}\right)}. \quad (\text{A.10})$$

In the derivations in section 2.4.4 the Gaussian model $\exp\left[\frac{-(f-f_\alpha)^2}{2\sigma^2}\right]$ was used. The terms σ and c relate to each other by

$$\sigma = \frac{1}{\sqrt{2}}c. \quad (\text{A.11})$$

REFERENCES

- [1] R. S. C. Cobbold, *Foundations of Biomedical Ultrasound*. New York, NY: Oxford University Press, 2007.
- [2] M. F. Insana, R. F. Wagner, D. G. Brown, and T. J. Hall, “Describing small-scale structure in random media using pulse-echo ultrasound,” *The Journal of the Acoustical Society of America*, vol. 87, no. 1, pp. 179–192, January 1990.
- [3] J. Mamou, M. L. Oelze, W. D. O’Brien Jr., and J. F. Zachary, “Extended three-dimensional impedance map methods for identifying ultrasonic scattering sites,” *Journal of the Acoustical Society of America*, vol. 123, no. 2, pp. 1195 – 1208, February 2008.
- [4] J. C. Bamber, *Physical Principles of Medical Ultrasound*. Chister, England: John Wiley & Sons, Inc., 2004, ch. Attenuation and Absorbtion, pp. 92–166.
- [5] L. X. Yao, J. A. Zagzebski, and E. L. Madsen, “Backscatter coefficient measurements using a reference phantom to extract depth-dependent instrumentation factors,” *Ultrasonic Imaging*, vol. 12, pp. 58–70, January 1990.
- [6] H. Kim and T. Varghese, “Hybrid spectral domain method for attenuation slope estimation,” *Ultrasound in Medicine & Biology*, vol. 34, no. 11, pp. 1808–1819, November 2008.
- [7] R. Kuc, M. Schwartz, and L. Von Kicsky, “Parametric estimation of the acoustic attenuation coefficient slope for soft tissue,” in *1976 Ultrasonics Symposium Proceedings*, 1976, pp. 44 – 7.
- [8] L. E. Kinsler, A. R. Frey, A. B. Coppens, and J. V. Sanders, *Fundamentals of Acoustics*. New York, NY: John Wiley & Sons, Inc., 1999.
- [9] A. Ishimaru, *Wave Propagation and Scattering in Random Media*. New York, NY: Academic Press, 1978.

- [10] V. Anderson, "Sound scattering from a fluid sphere," *Journal of the Acoustical Society of America*, vol. 22, pp. 426–431, July 1950.
- [11] J. Faran, Jr., "Sound scattering by solid cylinders and spheres," *Journal of the Acoustical Society of America*, vol. 23, no. 4, pp. 405–418, July 1951.
- [12] J. W. Strutt, "Investigation of the disturbance produced by a spherical obstacle on the wave of sound," *Proc. London Math. Soc.*, vol. 4, pp. 233–283, November 1872.
- [13] R. Chivers and C. Hill, "Ultrasonic attenuation in human tissue [measurement method]," *Ultrasound in Medicine & Biology*, vol. 2, no. 1, pp. 25–9, September 1975.
- [14] J. Bamber, M. Fry, C. Hill, and F. Dunn, "Ultrasonic attenuation and backscattering by mammalian organs as a function of time after excision," *Ultrasound in Medicine & Biology*, vol. 3, no. 1, pp. 15 – 20, November 1977.
- [15] M. Fink, F. Hottier, and J. Cardoso, "Ultrasonic signal processing for attenuation measurement: Short time fourier analysis," *Ultrasonic Imaging*, vol. 5, no. 2, pp. 117–135, April 1983.
- [16] A. Haak, Z. T. Hafez, J. J. Anderson, M. T. Herd, E. L. Nam, K. Madsen, T. A. Bigelow, T. J. Hall, and W. D. O'Brien, "Algorithm for estimating the attenuation slope from backscattered ultrasonic signals," in *Proceedings Ultrasonics Symposium*, 2009, pp. 1946 – 1949.
- [17] R. Kuc, "Generating a minimum-phase digital filter model for the acoustic attenuation of soft tissue," in *Proceedings Ultrasonics Symposium*, 1983, pp. 794–796.
- [18] K. A. Wear, T. A. Stiles, G. R. Frank, E. L. Madsen, F. Cheng, E. J. Feleppa, C. S. Hall, B. S. Kim, P. Lee, W. D. O'Brien Jr., M. L. Oelze, B. I. Raju, K. K. Shung, T. A. Wilson, and J. R. Yuan, "Interlaboratory comparison of ultrasonic backscatter coefficient measurements from 2 to 9 mhz," *Journal of Ultrasound in Medicine*, vol. 24, no. 9, pp. 1235–1250, April 2005.
- [19] K. Raum and W. D. O'Brien Jr., "Pulse-echo field distribution measurement technique for high-frequency ultrasound sources," *IEEE Transactions on Ultrasonics, Ferroelectrics, and Frequency Control*, vol. 44, no. 4, pp. 810–815, July 1997.